nature energy

Article

https://doi.org/10.1038/s41560-023-01414-5

Origin of fast charging in hard carbon anodes

In the format provided by the authors and unedited

Table of contents

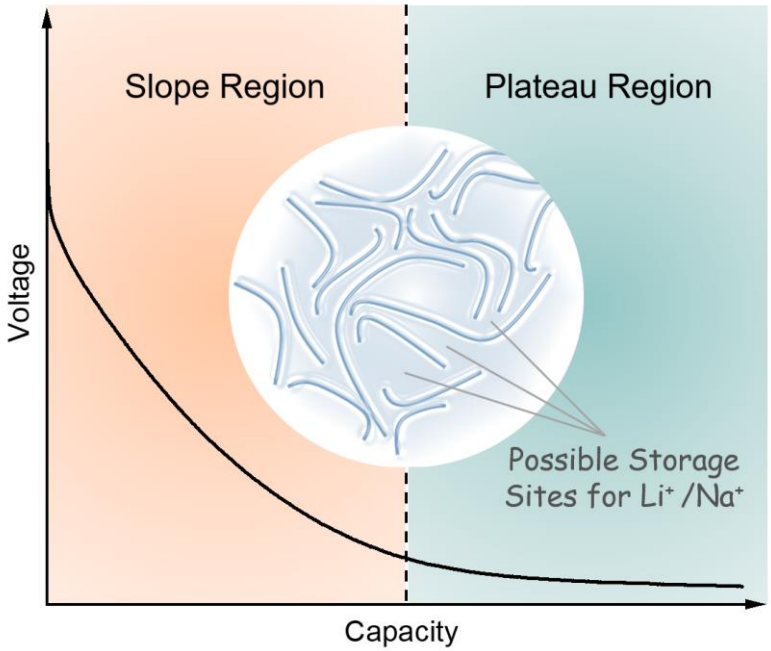

Supplementary Figure 1 | Typical electrochemical curves of hard carbon for LIBs and NIBs. Hard carbons usually exhibit a disordered structure[1]. The different explanations for the origin in the two voltage regions have led to a controversy about the storage mechanism. More specifically, mechanisms of "intercalation-pore filling", "adsorption-intercalation", "adsorption-pore filling", and "adsorption-intercalation-pore filling", have been proposed.

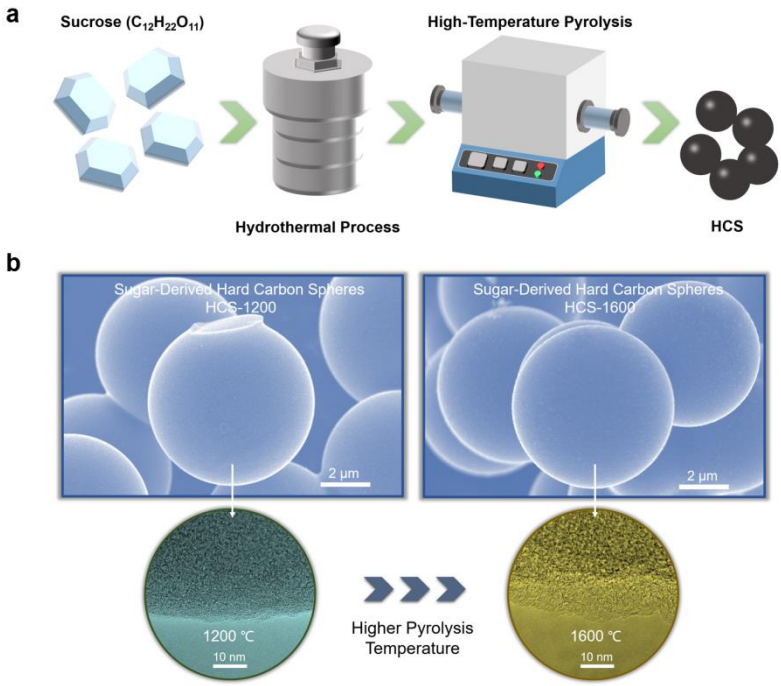

Supplementary Figure 2 | Schematic of the material synthesis for HCSs. a, scanning electron microscopy (SEM) of HCSs. b, transmission electron microscopy (TEM) of HCSs. HCSs with a regular spherical morphology, sized ~6 μm as determined by SEM, were obtained. Although both samples demonstrate the turbostratic microstructures, TEM analysis captured the fine structural differences between HCS-1200 and HCS-1600: HCS-1600 possesses longer microcrystal stripes and more closed nanovoids (flat geometry) than HCS-1200 due to the rearrangement of carbon atoms and folding of curved carbon layers, respectively. However, note that no perpendicular-oriented layers are observed in both samples. Considering these "layers" are highly defective and disordered structures, the curved lines observed in TEM micrographs may be the surface of (highly defective) graphene-like layers or chains of cyclic carbons rather than the edges of graphene layers[2].

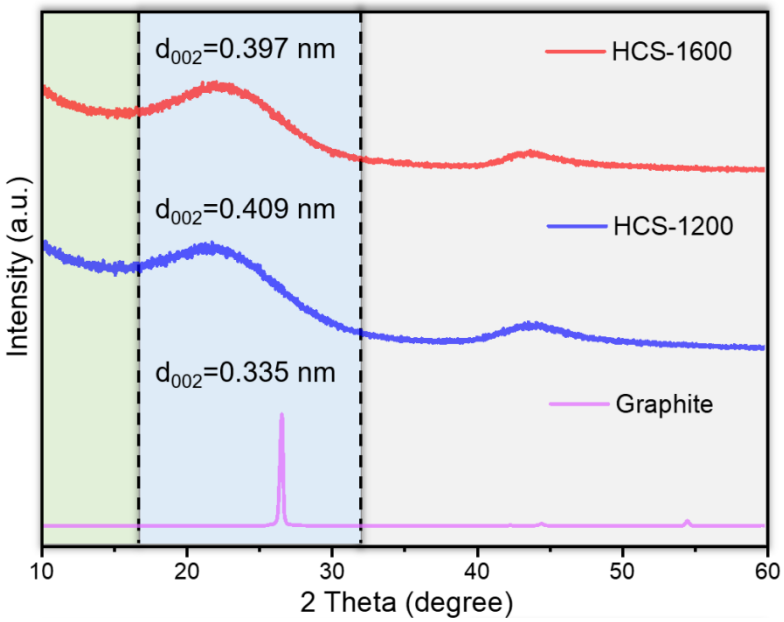

Supplementary Figure 3 | X-ray diffraction (XRD) of HCS-1200, HCS-1600, and graphite. Compared with the graphite sample, the broad peaks in the XRD patterns indicate amorphous structures of HCSs with a broad distribution in interlayer spacing. The average d-spacing of the graphene layer (d_{002}) slightly decreases to 0.397 nm from 0.409 nm, as determined from the (002) peak shift with increasing carbonization temperature.

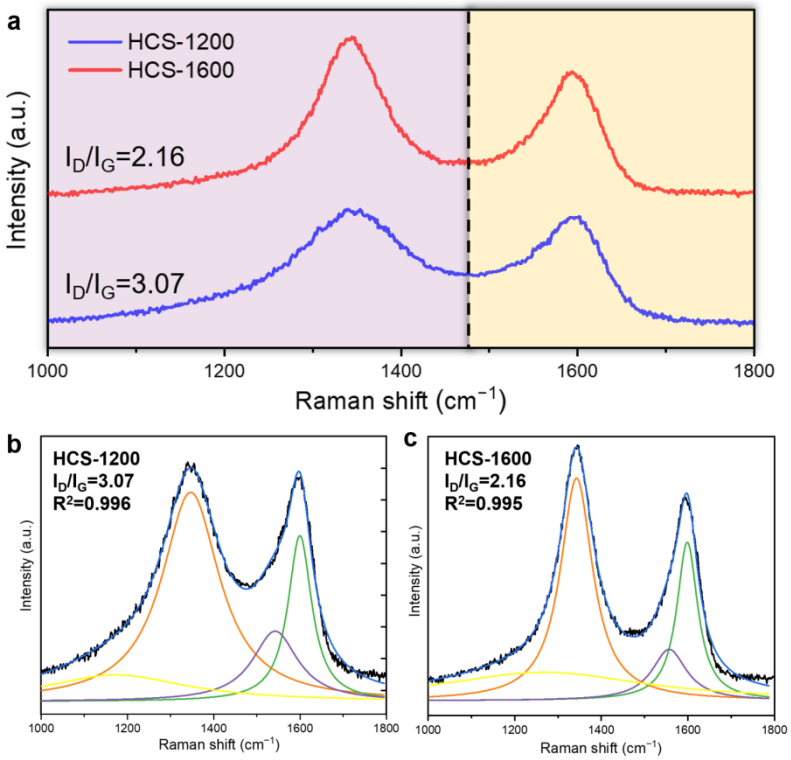

Supplementary Figure 4 | a, Raman spectra of HCS-1200 and HCS-1600. b,c, Fitted Raman spectra of HCSs based on Lorentz function. The Raman spectra are divided into four bands, i.e., D4-, D1-, D3-, and G-bands (from small to large Raman shift respectively).[3] R^2 is coefficient of determination. Raman spectra confirm that the integrated intensity ratio of the D1-band over the G-band (I_D/I_G) decreases from 3.07 to 2.16 with increasing carbonization temperature based on Lorentz fit, which suggests the reduction of defects. Thus TEM, XRD and Raman results all indicated a slight ordering of the carbon structure as the carbonization temperature increases. Nevertheless, even at the highest carbonization temperature these structures are not dominated by the layered carbon structure.

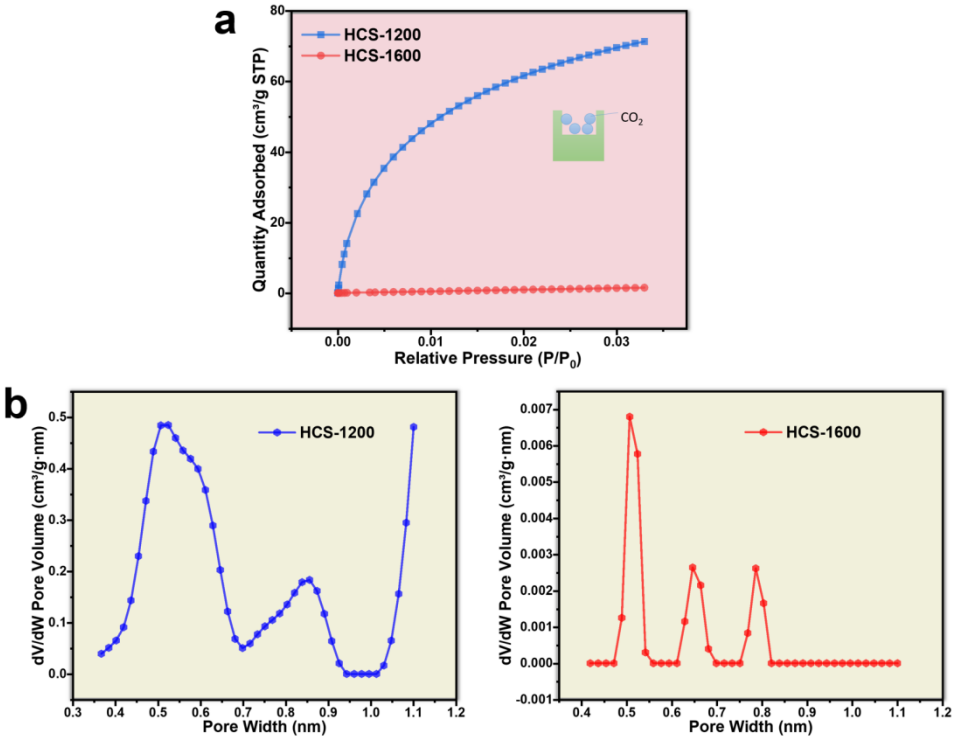

Supplementary Figure 5 | a, CO_2 adsorption isotherms. b, The corresponding nonlocal density functional theory (NLDFT) pore size distribution. Note that the up-turned tails at the low angle region (10-15°) of XRD results of HCSs and an abnormal increase of D-band of HCS-1600 both reveal the existence of a microporous structure in HCSs, motivating detailed pore structure analysis. It can be seen that HCS-1200 presents a higher CO_2 adsorption volume than HCS-1600. Based on the Dubinin-Astakhov model[4], the micropore surface areas of HCS-1200 and HCS-1600 are 481 m^2/g and 102 m^2/g, respectively. Moreover, the average size of pores of HCSs decreases and there are more intense peaks of pore size distribution with the increase of carbonization temperature.

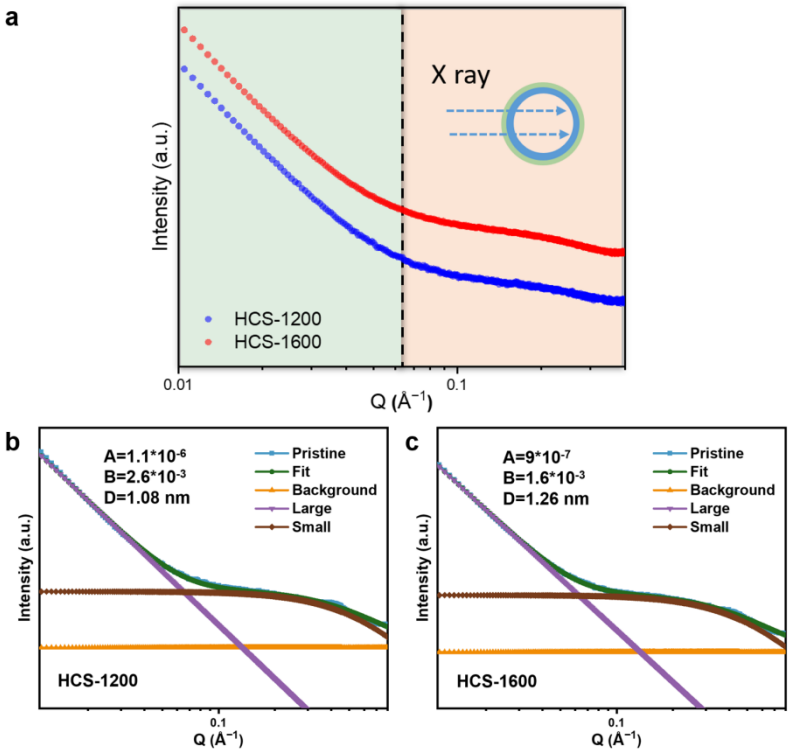

Supplementary Figure 6 | a, SAXS patterns of HCSs. b,c, fitted SAXS patterns of HCSs. Considering that CO_2 adsorption can mainly provide the open pore surface area, small angle X-ray scattering (SAXS) and skeletal (true) density analysis were employed to analyze the closed pores of HCSs. There is a broad peak around q ≈ 0.1 Å^{-1} in both SAXS patterns of HCSs, indicating a distribution of closed nanopores. The fitted model is based on the previous paper[5], A and B are proportional to the total surface areas of the large and small pores, respectively. D is the diameters of closed nanopores. Based on the spherical closed pore model the characteristic length related to the scattering power variation was fitted, revealing an increase of average diameter of closed pore from 1.08 to 1.26 nm with increasing pyrolysis temperature from 1200 to 1600 °C.

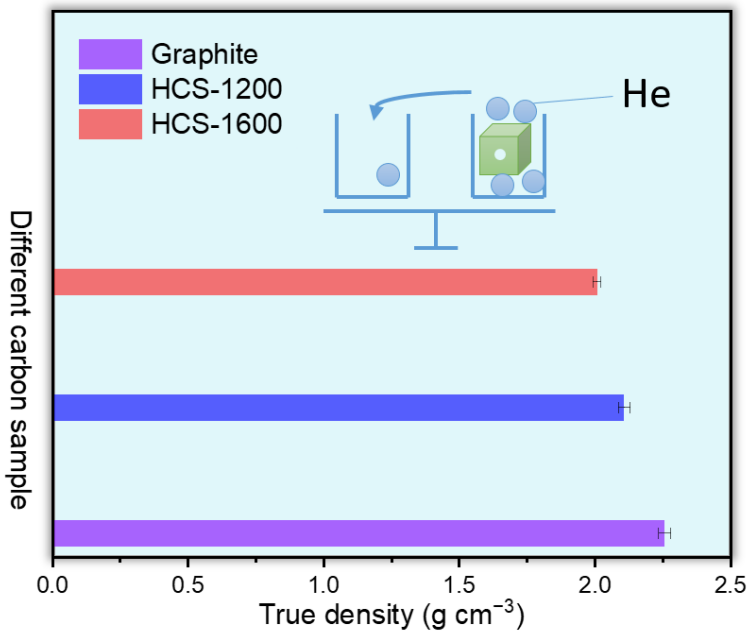

Supplementary Figure 7 | Skeletal density tests using He of HCSs. We used helium (He) as the probe (degassing way) to make skeletal density analysis. The error bar (standard deviation) of skeletal density data was obtained by three samples from different batches. The average used is the mean value. The data of this Figure are presented as the mean values ± standard error of the mean.

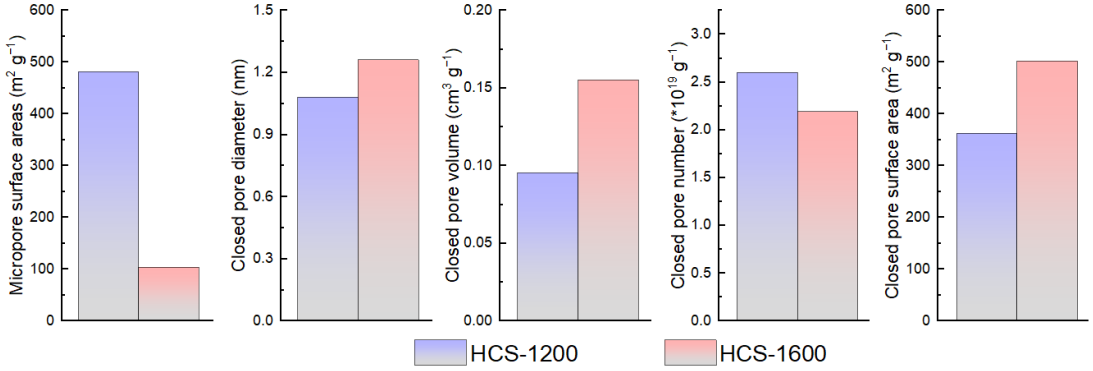

Supplementary Figure 8 | Open/closed pore structure information. It can be seen that the HCS-1600 sample has lower skeletal density and higher closed pore volume than those of HCS-1200, considering the skeletal density value of graphite without closed pores as the theoretical baseline. The closed pore number and surface area can be obtained assuming that all closed pores are uniform spheres in our previous paper[6]. The actual closed pores in HCSs may have a wedge shape (flat geometry) built by the graphene layer. Thus, further considering the crystallite sizes L_a (HCS-1600: 8.90 nm; HCS-1200: 6.26 nm) from I_D/I_G[7], a wedge-pore (like triangle) model was proposed to calculate the closed pore number and surface area. It can be seen that closed pore number decreases, but volume and surface area increases with the carbonization temperature increasing.

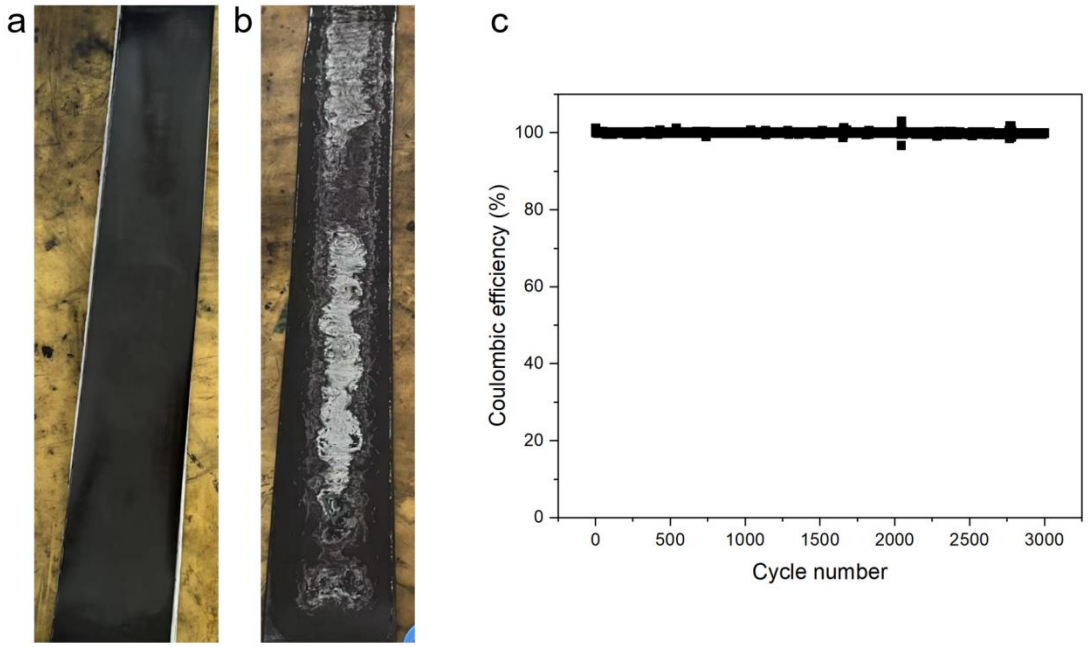

Supplementary Figure 9 | a, Digital picture of HCS-1200 after 3000 cycles of 26700-type full-cells under 6.5C rate (charging to 4 V). b, Digital picture of Na deposition on HCS-1200 via overcharging of 26700-type full-cells. The electrode width of both is 64 mm. c, Coulombic efficiency plot of 26700-type full-cells under 6.5C rate during cycling. The Coulombic efficiency is very stable and shows a high average value of ~99.93% during 3000 cycles. Such a high and stable Coulombic efficiency cannot be achieved if there is sodium deposition. It is well-known that Na is very active towards liquid electrolytes. Thus, we can confirm there is no Na dendrite.

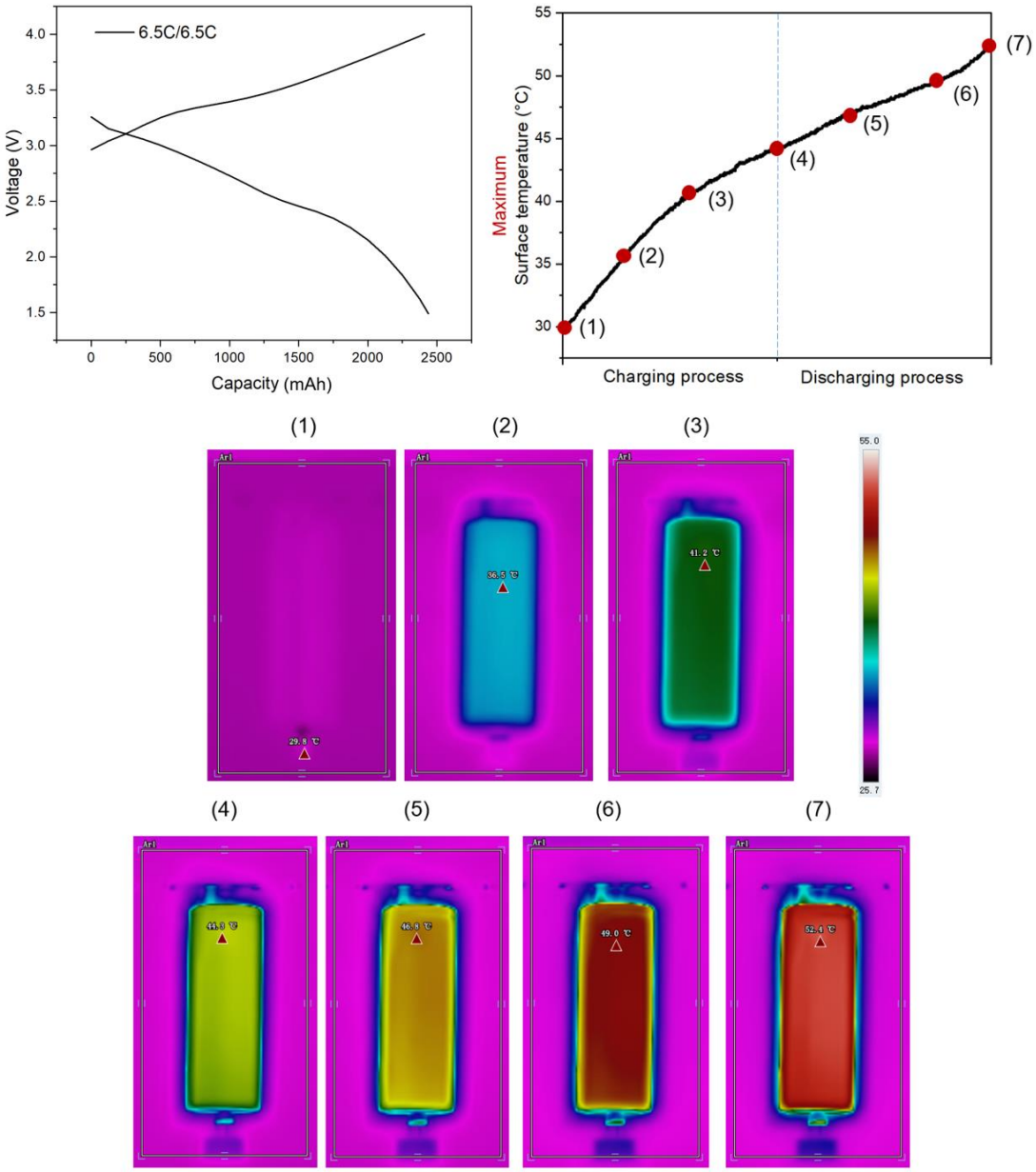

Supplementary Figure 10 | The electrochemical curve of 26700-type cell during fast charging-discharging at 6.5C and corresponding selective points of in-situ thermal imaging of surface temperature change. The monitoring point of thermal imager focuses on the center of the cylindrical cell in the radial direction. The red arrow indicates the point with the highest temperature within the selected box of Ar1. For the temperature change test, there is no large convection cooling used[8]. The small internal heat generation[9] is due to a small internal resistance in our system.

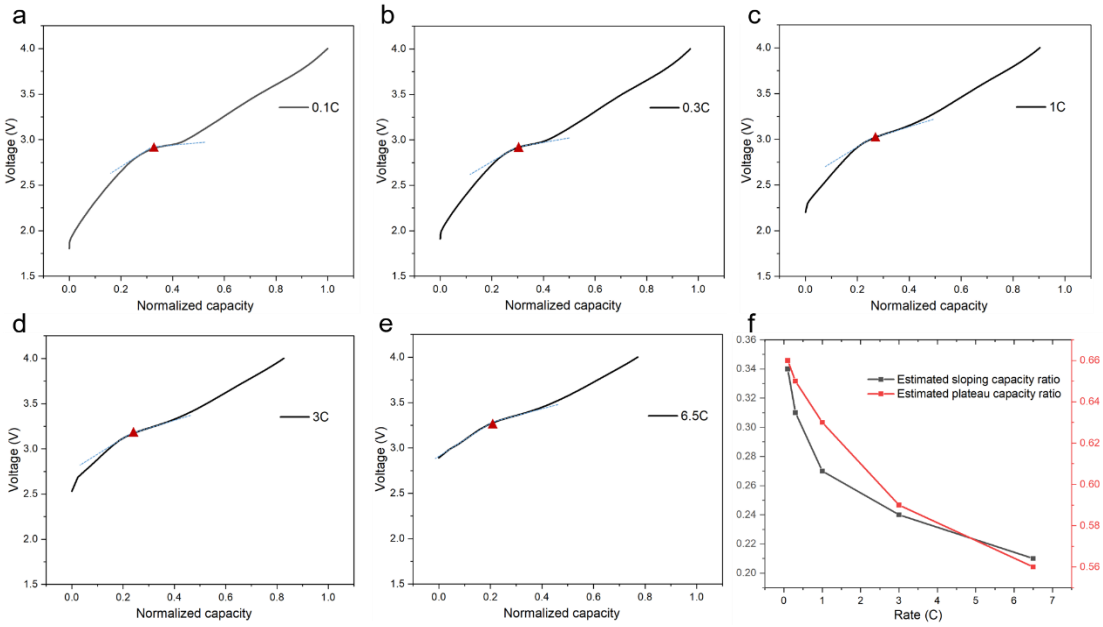

Supplementary Figure 11 | a-e, Galvanostatic charge curves of 26700-type $Na[Cu_{1/9}Ni_{2/9}Fe_{1/3}Mn_{1/3}]O_2$//HCS-1200 Na-ion full cell at different rates. By adding trend lines at the inflection point (triangle mark) of charging process, the intersection of the two trend lines can be roughly considered as the junction of the sloping and plateau region. f, Relation curve of C-rates and estimated sloping/plateau capacity ratio.

In the discharging curve of half-cell (Figure 2), the sloping region approximately occupies ~30% of total capacity thus we define the first 30% capacity in the full cell (0.1C) belongs to the sloping storage of hard carbon while the left is related to the plateau region. It can be observed in Figure S11a, the intersection of two trend lines at the inflection point (The slope of the curve changes significantly) of the charging process is exactly the junction of sloping and plateau region. Thus, we can obtain sloping and plateau capacity changes at different C-rates. It can be seen that both sloping and plateau capacities suffer a decay under high-C-rates and there is a similar decay rate in Figure S11b-S11f. The phenomenon illustrates plateau region has similar tolerance with sloping region against fast charging in our hard carbon, indicating the adsorption barrier of defects is similar with that at well-designed closed pore surface (under-potential-deposition is also like a adsorption process). Therefore, it is feasible to achieve the fast charging performance through improving the dynamics of the plateau

region. In this work through optimizing the closed pore size, we realized good kinetics adsorption process of the plateau region, where only ~23% total capacity loss under 6.5C rate (vs. 0.1C).

Note that we mainly focus on the sodiation process in hard carbon in this work. Sodiation process occurs during discharge in the half cells with Na metal as the counter electrode while sodiation process occurs during charge in the full cells with layered oxide as the counter electrode.

In our work, we used large-size cylindrical cells with highly encapsulated roll-to-roll electrodes inside. Thus, it is very challenging to perform three-electrode testing in this kind of cylindrical batteries because there is no extra space. Trend lines can provide us with a non-destructive analysis technique and can roughly give the trend of plateau and slope capacity change. But considering the cathode polarization, this kind of trend line method may not give the accurate values. Further development of a three-electrode device for the cylinder NIBs is also required in the future.

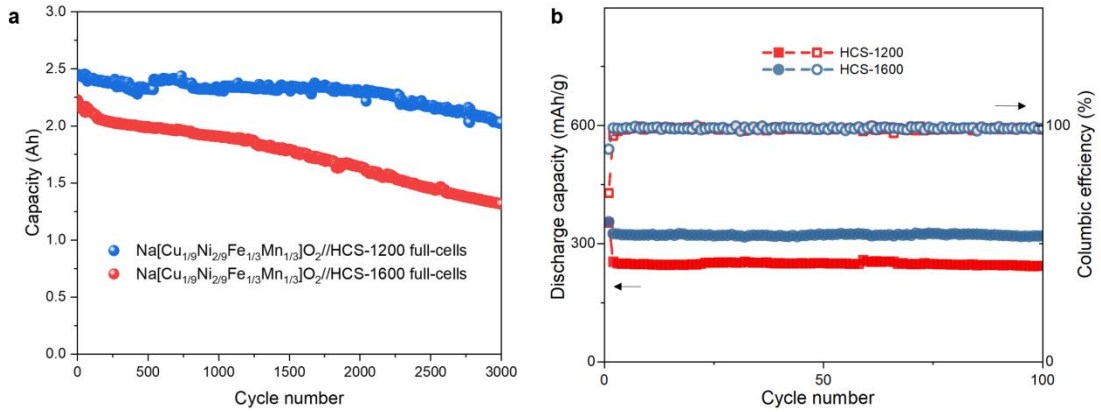

Supplementary Figure 12 | a, Cycling performances of $Na[Cu_{1/9}Ni_{2/9}Fe_{1/3}Mn_{1/3}]O_2$||HCS-1200 and $Na[Cu_{1/9}Ni_{2/9}Fe_{1/3}Mn_{1/3}]O_2$||HCS-1600 NIBs at a current rate of 6.5C. b, Cyclic capability of Na-based half-cells with HCSs at a current rate of 0.1C between 0-2 V.

It is found that the HCS-1200-based full cell provides the higher capacity than that of HCS-1600 (2.4 Ah vs. 2.2 Ah) under higher rate of 6.5C and demonstrates higher capacity retention after 3000 cycles (83% vs. 60%) at 6.5C, as shown in Figure S12a. Actually, both full cells based on HCS-1200/1600 have good fast charging properties while the HCS-1200-based one is better.

We further provide the half-cell performance of HCS-1200 and HCS-1600 with coin-type cell, and their cycling performance is shown in Figure S12b. To be mentioned that the half-cell configuration is mainly used to evaluate the capacity of carbon but its long cycling and fast charging properties are usually weakened by the influence from active Na metal[10, 11]

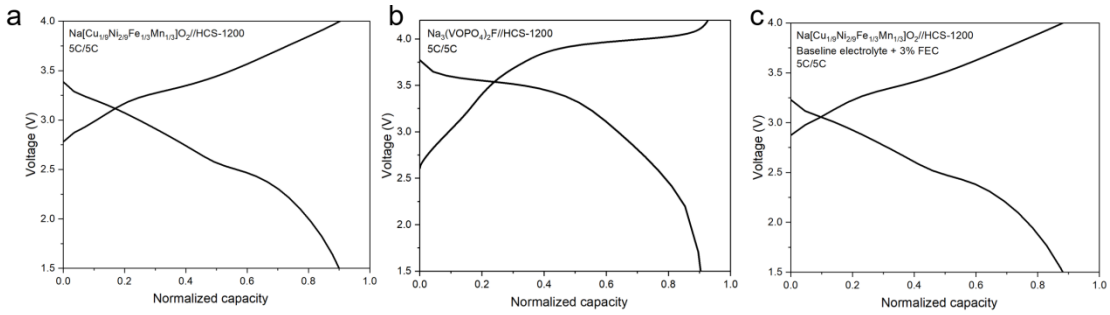

Supplementary Figure 13 | Galvanostatic charge/discharge curves of different cylindrical Na-ion full cell at 5C rate. Concerning the origin of fast-charging performance, all the cathode, anode and electrolytes have effects on the kinetics, however, the main limiting factor or key design factor is anode side for Na-ion batteries, which is similar with commercial Li-ion batteries with graphite anode[12]. We performed some supplementary tests to confirm the above. As shown in Figure S13a, real capacity is normalized based on the capacity of battery under 1C/1C rate. It is convenient to intuitively understand the battery capacity retention under high-C-rate. In Figure S13b and S13c, polynomic $Na_3(VOPO_4)_2F$ is selected as the new cathode and 1M $NaPF_6$ in EC/DEC/PC + 3% FEC is prepared as the new electrolyte, respectively. It is found that their capacity retentions are similar to that of baseline full cell under 5C/5C rate in Figure a. Thus the influence of cathode or electrolyte is relatively weak.

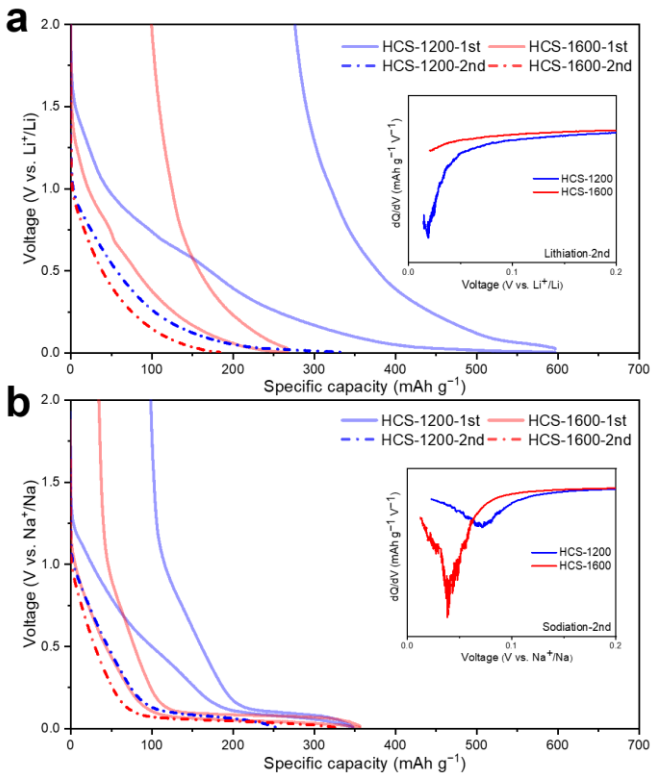

Supplementary Figure 14 | Galvanostatic initial discharge/charge curves and second discharge curves at a current rate of 15 mA g^{-1} in (a) LIBs and (b) NIBs, respectively. Inset: related differential capacity curves.

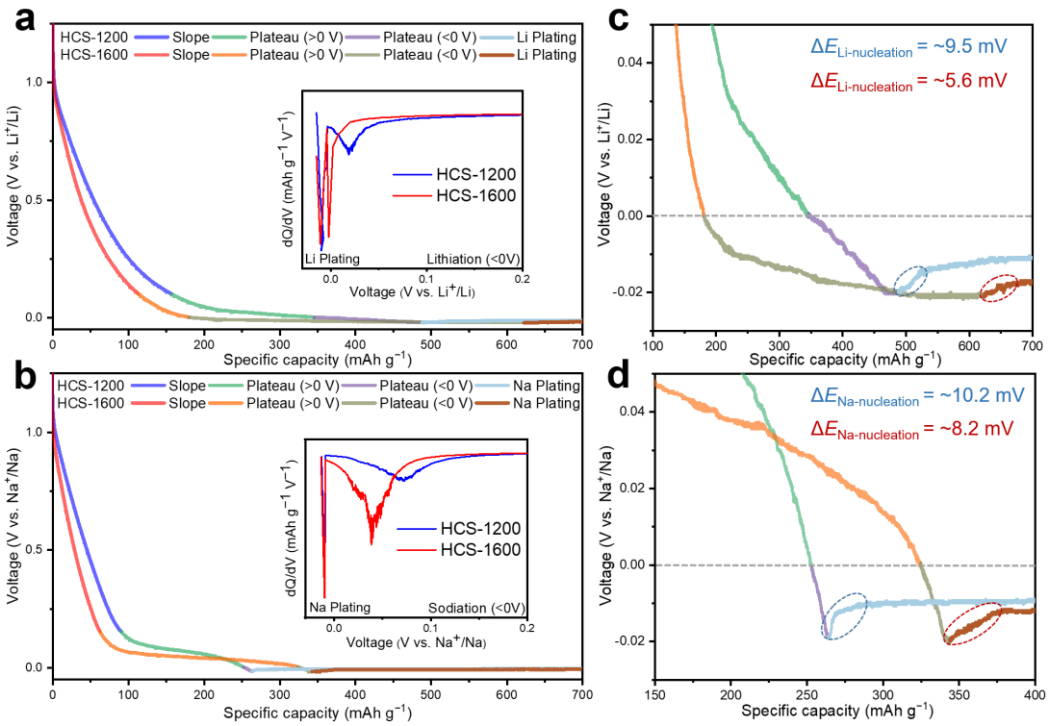

Supplementary Figure 15 | a,b, Galvanostatic discharge curves (<0 V) at a current rate of 15 mA g^{-1} in LIBs and NIBs, respectively. Inset: related differential capacity curves. c,d, Detailed curves below 0 V and the nucleation overpotentials (the red circles indicate the nucleation process).

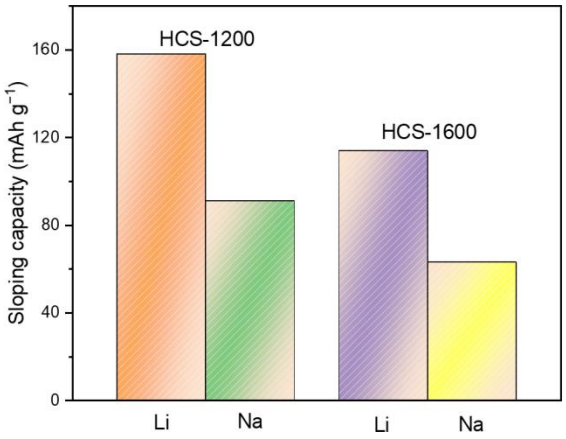

Supplementary Figure 16 | Sloping capacities of HCSs for Li (2-0.1 V) or Na (2-0.15 V) storage.

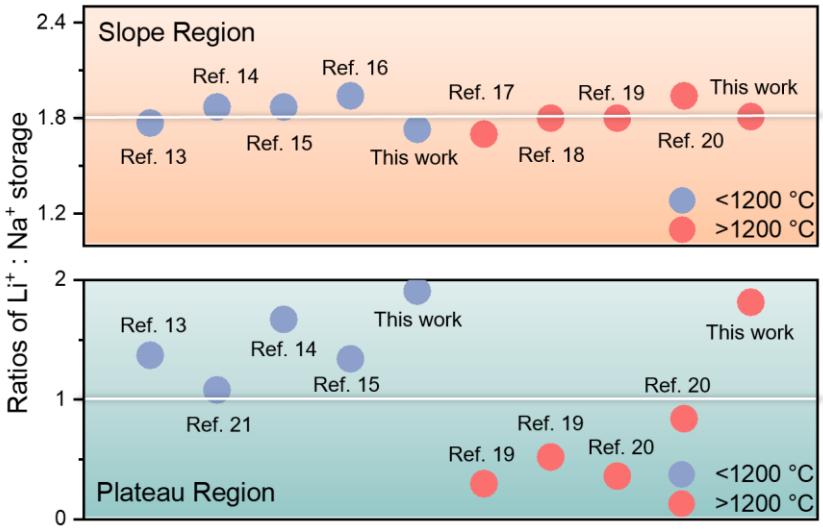

Supplementary Figure 17 | The Summary of ratios of Li/Na storage capacity in hard carbon with the increase of pyrolysis temperature from the previous reports[13, 14, 15, 16, 17, 18, 19, 20, 21] and this wok. Note that Carbotron P(J) (pyrolysis temperature: 1000-1500°C) used in ref. 17 and 18 is classified as >1200°C.

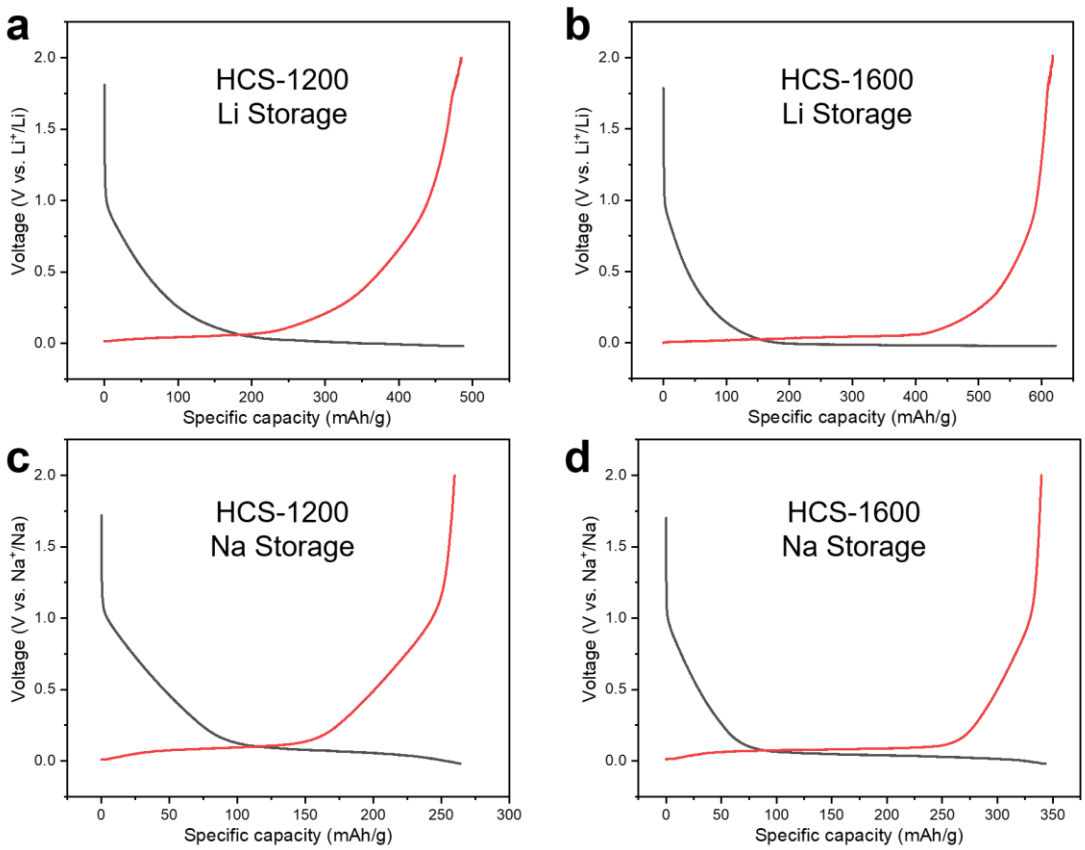

Supplementary Figure 18 | The verification about the reversibility of below 0 V but before plating (stop overdischarge just before "V" shape), which is related to the second cycle at a current rate of 0.05C. Note that the sodiation-desodiation process in hard carbon is highly reversible and the charge-discharge curve is also approximately symmetrical.

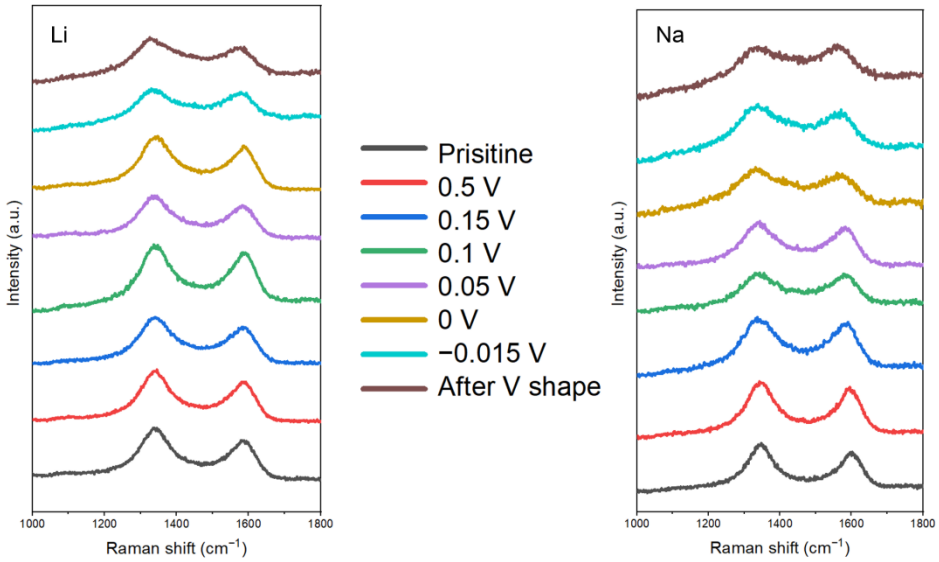

Supplementary Figure 19 | In situ Raman spectra of HCS-1600 during lithiation and sodiation.

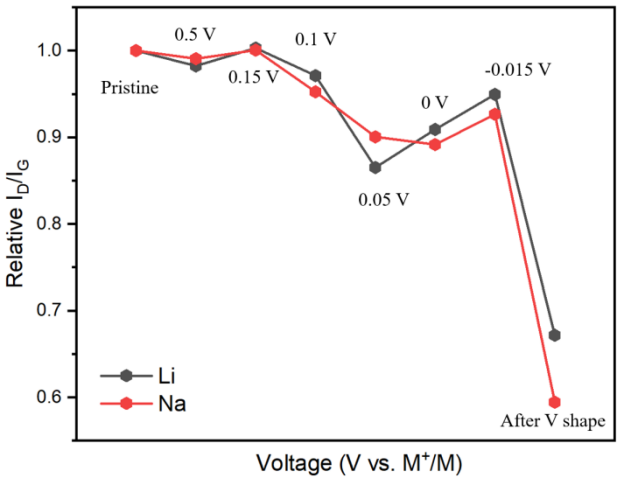

Supplementary Figure 20 | I_D/I_G analysis from In situ Raman spectra. In situ Raman tests in Supplementary Figure 19 revealed that there is no peak splitting of the D- or G-band and no new peak appears in both sloping and plateau region, indicating that Li^+ and Na^+ do not intercalate into the layers of carbon. The slight peak shift of G-band may lie in the electrons occupying the Π* anti-bonding band of carbon layers induced by charge transfer effects from the adsorption of Li^+/Na^+.[22] The integrated intensity ratios of the D1-band over the G-band (I_D/I_G) can be further calculated (Supplementary Figure 21). The I_D/I_G values show nearly no variation in the sloped voltage region, suggesting a relatively weak interaction between Li/Na and HCSs. However, the I_D/I_G values suffer a decay at the voltage range of 0.15 V-0.05 V for both Li and Na, indicating that Li^+ or Na^+ could enter the closed pores through the defects. The above phenomenon may be a shielding behavior that ions pass through the defects inducing a weakened D-band. In the plateau region, ions enter into the closed pores and the I_D/I_G values start rising until the Na plating process. The reversible change of relative intensity of the D-band suggests that passing through the defect paths will not destroy the original defects. Finally, the I_D/I_G values suffer a significant drop due to the formation of Na metal.

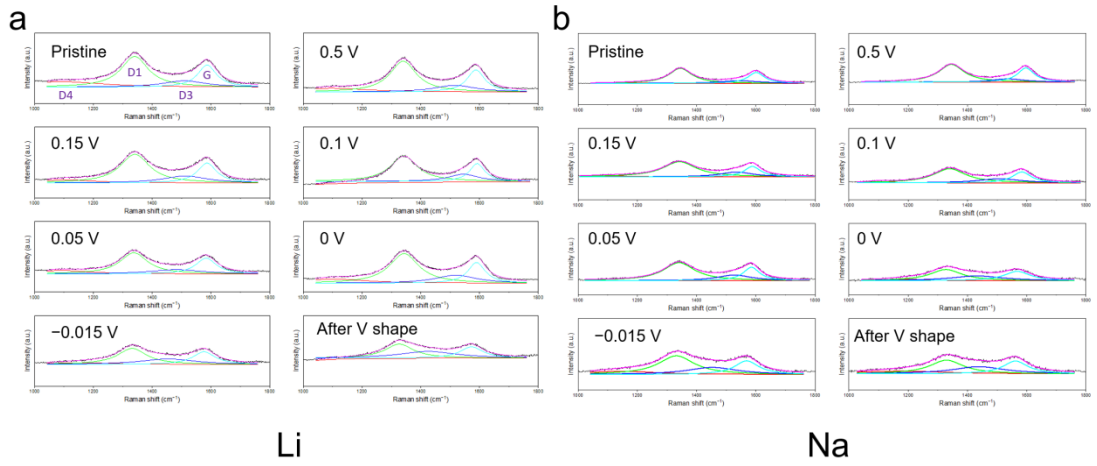

Supplementary Figure 21 | Fitted Raman spectra of different discharging states of HCS-1600 based on Lorentz function. The related Raman spectra are divided into four bands, i.e., D4-, D1-, D3-, and G-bands (from small to large Raman shift respectively).[3]

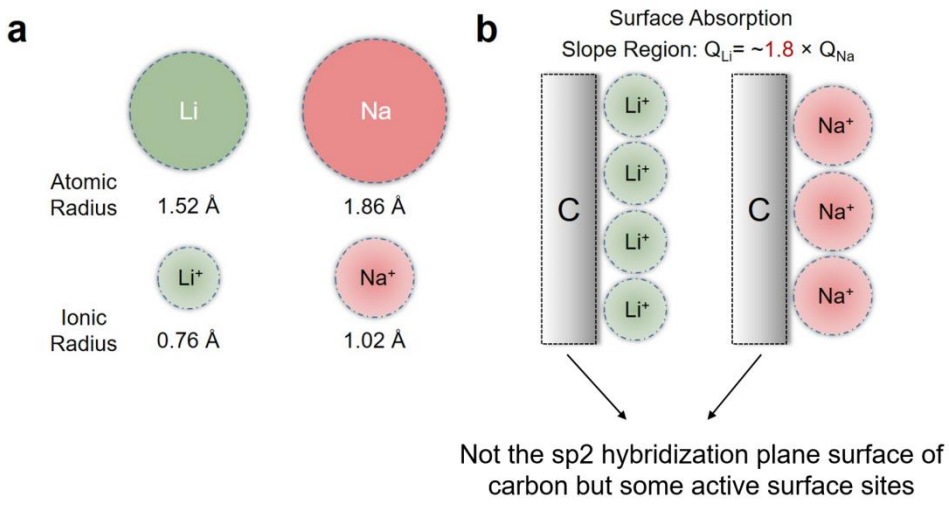

Supplementary Figure 22 | a, Atomic and ionic radius of Li and Na. b, Schematic of surface effect. The ratio of the ion projected area (based on the ion radius) of Na^+ to Li^+ equals 1.8. The smaller size of Li^+ allows more Li storage by adsorption on active surface sites (edges and vacancies) than that of Na^+.

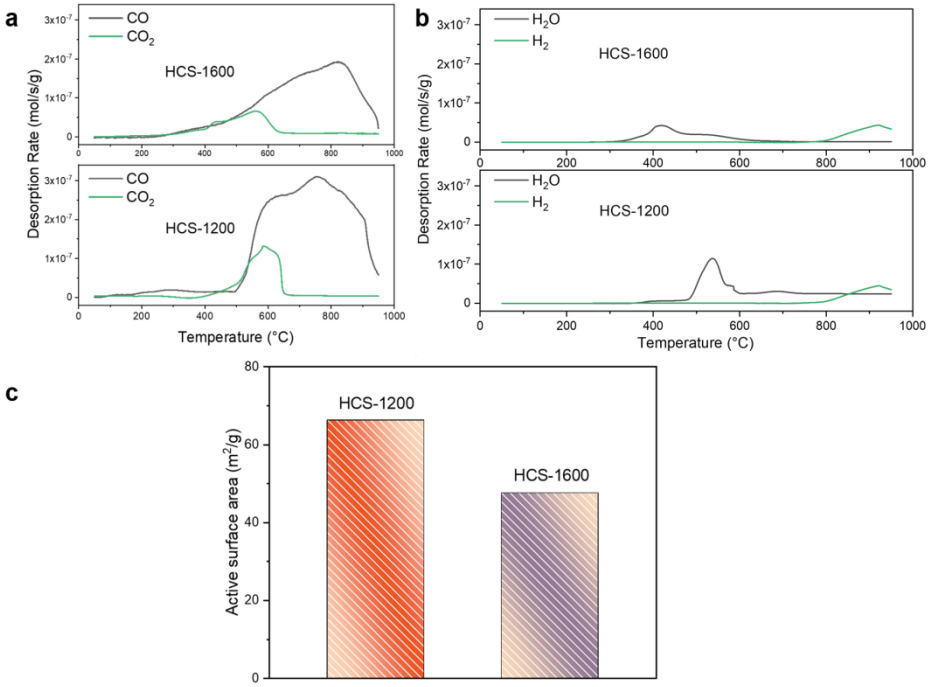

Supplementary Figure 23 | a,b, TPD-MS thermal desorption profiles (CO, CO_2, H_2O and H_2) for HCSs. c, The related active surface area of HCSs.

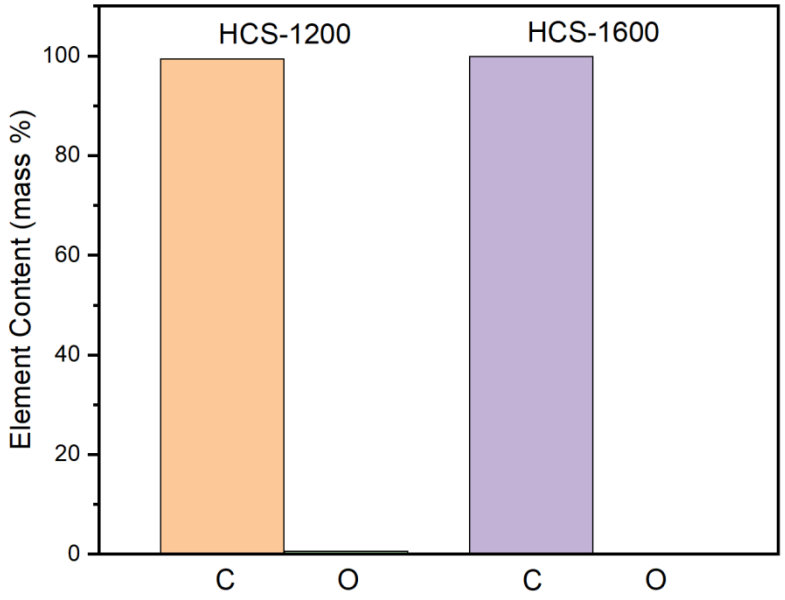

Supplementary Figure 24 | Elemental analysis for HCSs.

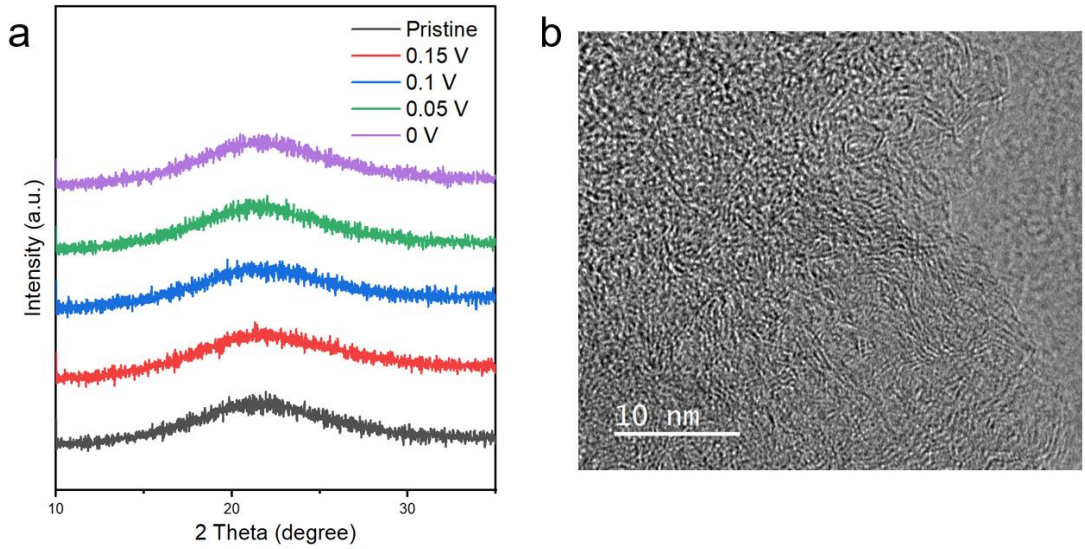

Supplementary Figure 25 | a, Ex situ XRD patterns of HCS-1200 during sodiation (second cycle). b, TEM image of HCS-1200 after discharging to 0 V (second cycle).

Ex situ XRD patterns in Figure a present that there is no obvious (002) peak shift at different discharge states, implying no intercalation of Na into graphitic layers at a wide voltage range due to the constant interlayer spacing. Ex situ TEM result in Figure b reveals that the fully sodiated HCS still exhibits a disordered carbon structure without crystal lattice stripes, which is similar to the pristine sample in Supplementary Figure 2. The d-spacing for both the pristine and sodiated sample is ~0.4 nm. Thus both XRD and TEM results can clearly confirm that the intercalation process does not happen in low-voltage region.

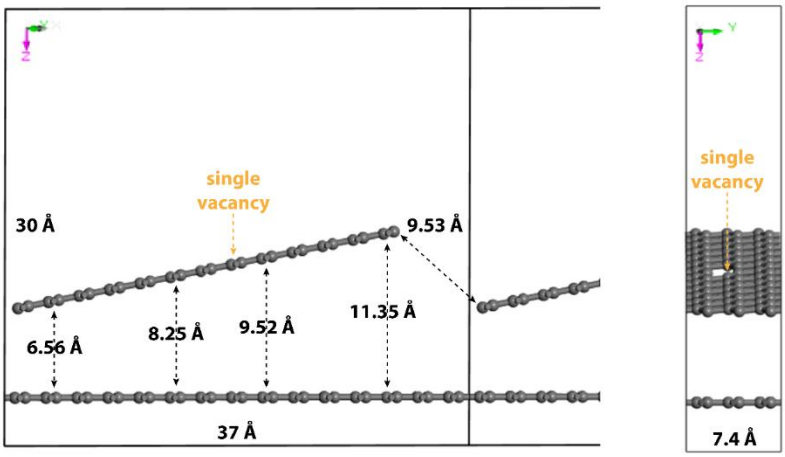

Supplementary Figure 26 | A wedge hole model for DFT calculations of plateau region.

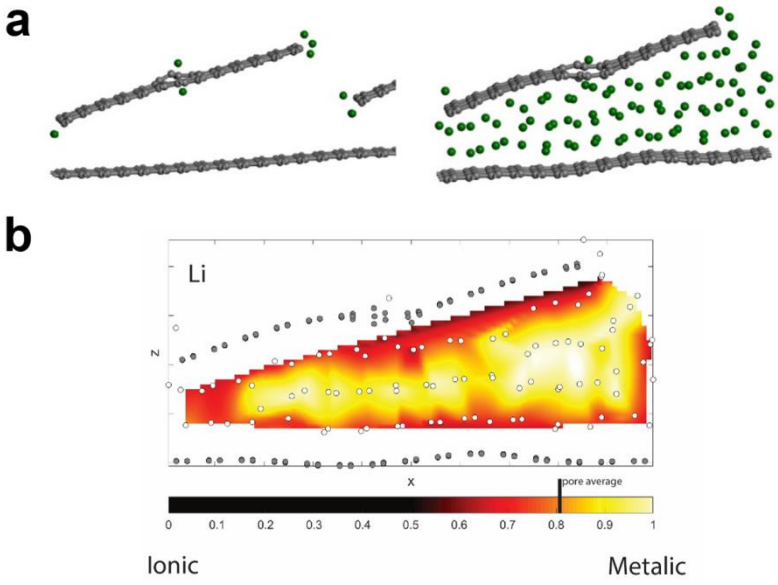

Supplementary Figure 27 | a, Lithiated configurations throughout the lithiation process. b, Electron density results of Li in the pore.

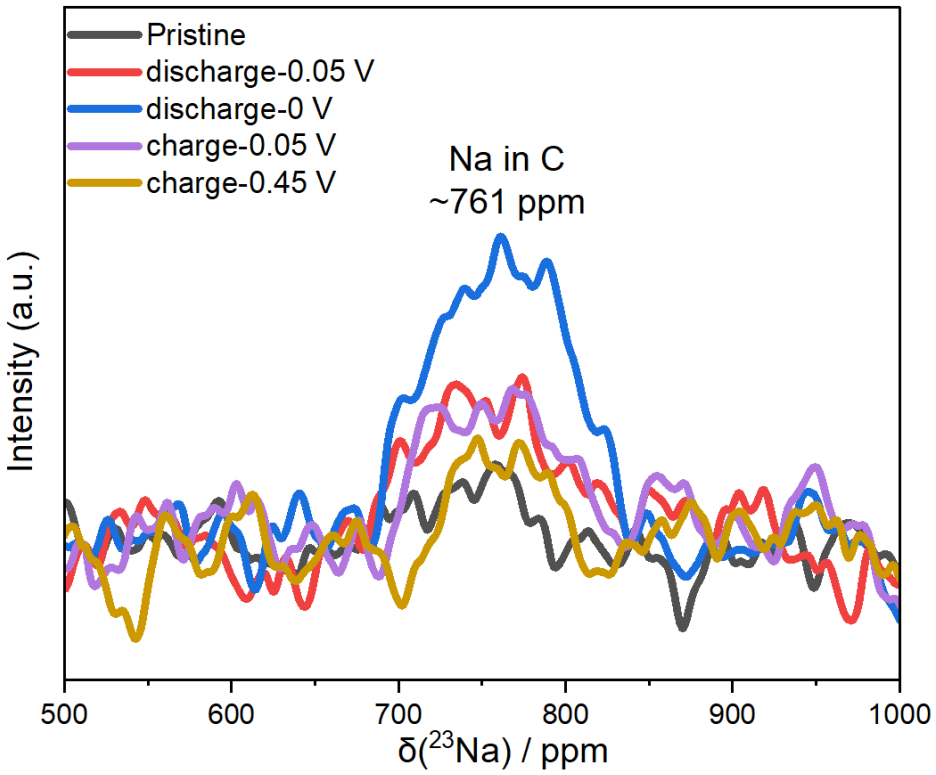

Supplementary Figure 28 | In situ 23Na NMR spectra for electrochemical cells with sodium metal and HCS-1200 electrode. It can be seen that the Na storage process is highly reversible. When discharging to 0 V the Knight shift of Na peak locates at ~761 ppm, far away from the ~1135 ppm of Na metal signal, indicating the quasi-metallic nature. We expect more obvious Knight shift (>761 ppm) would occur if the plateau capacity keep increasing.[23, 24]

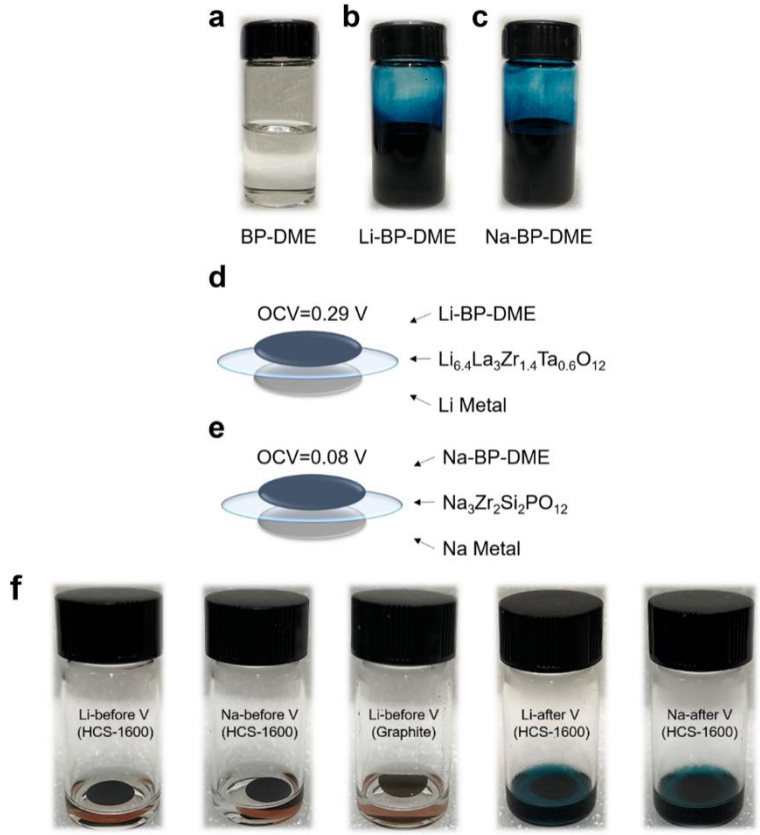

Supplementary Figure 29 | Preparation of titration experiments. a-c, Photographs of BP-DME, 1 M Li-BP-DME and 1 M Na-BP-DME solutions. d,e, Measurements of open circuit voltages of Li/Na-BP-DME through assembling the solid state batteries. f, Digital pictures about the reactions between BP-DME solution and HCS (and graphite) electrode with different discharged states.

In order to understand the intrinsic nature of Li/Na in closed pores, several ex situ tests with lithiated or sodiated HCS anodes were designed. Considering BP-DME can dissolve metallic Li/Na to become reducing agents with color changed[25], BP-DME was used as the chemical indicator to determine whether metallic Li/Na exist. To check if BP-DME can react with Li/Na in the low potential (plateau) region, open-circuit voltages of Li/Na-BP-DME were measured through assembling the solid-state batteries, and the respective 0.29 V and 0.08 V OCV for Li- and Na-based battery indicate the feasibility of the proposed method. HCS electrodes with different discharged states were put into BP-DME, and it was found that the fully Li/Na-inserted-HCS cannot change the solution's color, but the samples with Li/Na metal plating (after "V" shape) can change the color to dark blue. Moreover, Li-inserted graphite was also used as the

reference. Despite the low Li insertion voltage, the color of the solution did not change due to the ionic state of Li in graphite. The sample used in this Figure is HCS-1600, and the titration tests of lithiated or sodiated HCS-1200 are expected to have similar phenomenon because of their higher average potential and weaker metallic state is more difficult to change the color of BP-DME.

Note that the basic principle of our titration method is different from that of Wang's work[26]. Our work used biphenyl and dimethoxyethane (BP-DME) to probe the metallic Na considering that metallic Na and BP-DME tend to form dark green alkali solution known as radical anions [25]. But Wang's work is based on the chemical reaction between metallic sodium and a protic solvent (ethanol)[26]. More importantly, we have totally different conclusions from titration tests: we believed that there is no complete metallic state of Na in closed pores while they claimed that quasi-metallic Na was detected.

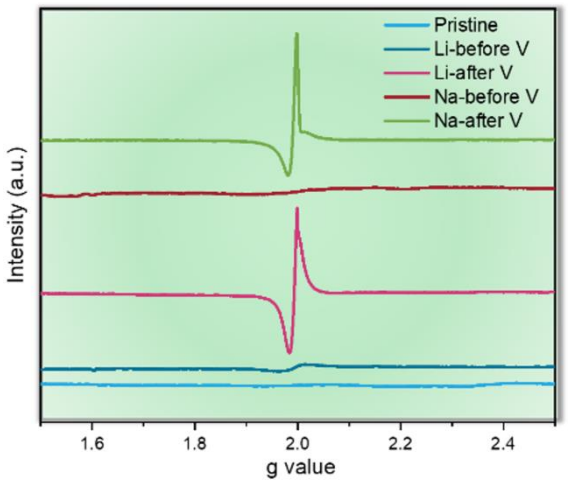

Supplementary Figure 30 | EPR spectra of the HCS-1600 electrode at different discharge states. It can be seen that the EPR curves of fully Li/Na-inserted-HCS-1600 are similar to that of the pristine HCS-1600, which didn't show obvious peaks. However, the samples with Li/Na metal plating induce the sharp asymmetric peak with Dysonian shape, indicating unpaired electrons[27].

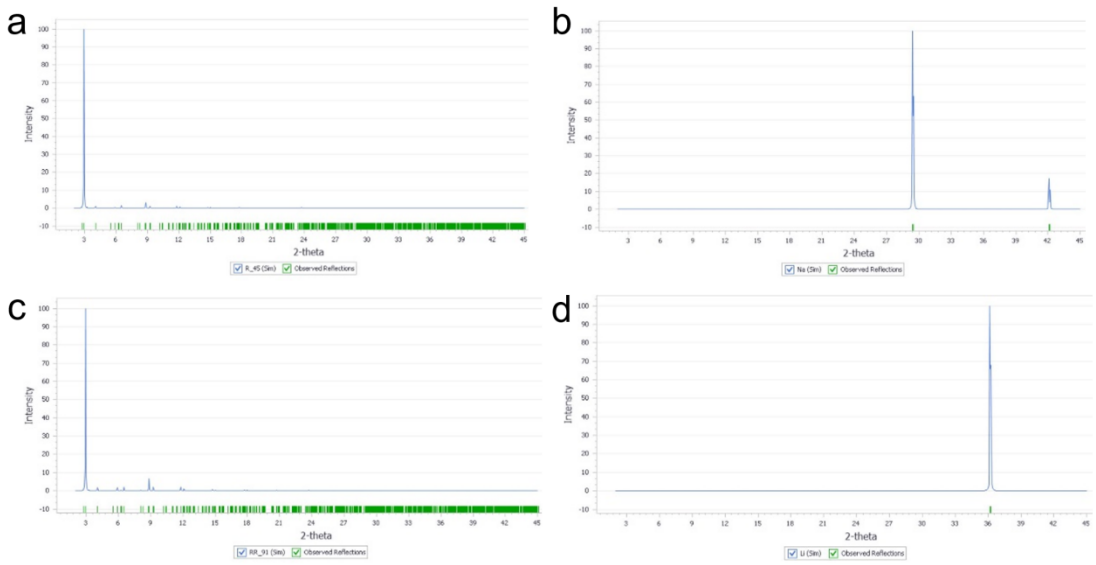

Supplementary Figure 31 | a, simulated XRD of fully sodiated pore. b, simulated XRD of Na metal. c, simulated XRD of fully lithiated pore. d, simulated XRD of Li metal. All simulations are performed assuming a Cu source. The peaks below 3 degrees in the pore configurations are a simulation artifact due to the periodicity of the supercell. The Li/Na atoms exist in an amorphous, quasi-metallic solid state inside the pores. We examine the interatomic distances being, on average, shorter than the metallic bonds. For example, the average distance for Na in a completely sodiated pore is 3.57 Å (Figure 3g), while the metallic crystalline Na lattice forms bonds of 3.7 and 4.2 Å in the (110) (100) directions, respectively. The above value indicates that the pore environment allows Na atoms to pack slightly closer than the metallic state as part of the electron density is donated to the carbon matrix. This is further supported by charge analysis showing that ~20% partial electron density donation to the carbon lattice. In theory, the configuration of the fully lithiated/sodiated pore should be closer to the crystalline phase; however, based on the realistic situation where only 2-3 Na or 3-4 Li layers are allowed in the pore, it is in an amorphous nature. We additionally simulated XRD patterns of the fully lithiated/sodiated pores, and no Li/Na crystalline peaks were located

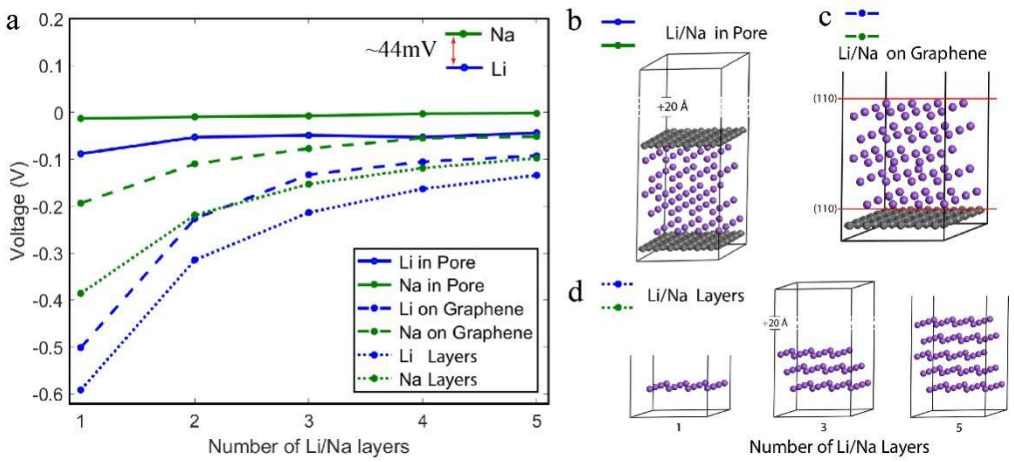

Supplementary Figure 32 | Simulated Li/Na surface effect, encapsulated configurations. a, voltage comparison between Li/Na layers (two exposed surfaces), Li/Na on graphene (1 exposed surface), Li/Na in the encapsulated pore (complete enclosure – no exposed surfaces). b,c,d, schematic representations of the respective configurations.

In agreement with experiments and literature, we find that the (110) surface energy is lower for Na than for a Li metal surface (Supplementary Table 1). Actually, the "V" shape for Na is sharper than that for Li, indicating that the nucleation overpotentials of Na metal deposition are larger than for Li (Figs. 2c and 2d), which is attributed to the lower surface energy of Na than Li (metal in vacuum).[28] The (110) surface selection is additionally determined to be the most favorable monolayer on graphene with DFT calculations. To evaluate how these surfaces contact the carbon structure, we calculated the plating potentials of Li/Na multilayer deposition on graphene sheets and subsequently added a second graphene layer completely encapsulating the Li/Na layers. Going from the metallic layers (2 exposed surfaces) to the encapsulated pore (0 exposed surfaces), we see that each Li/Na – graphene interface contact raises the voltage.

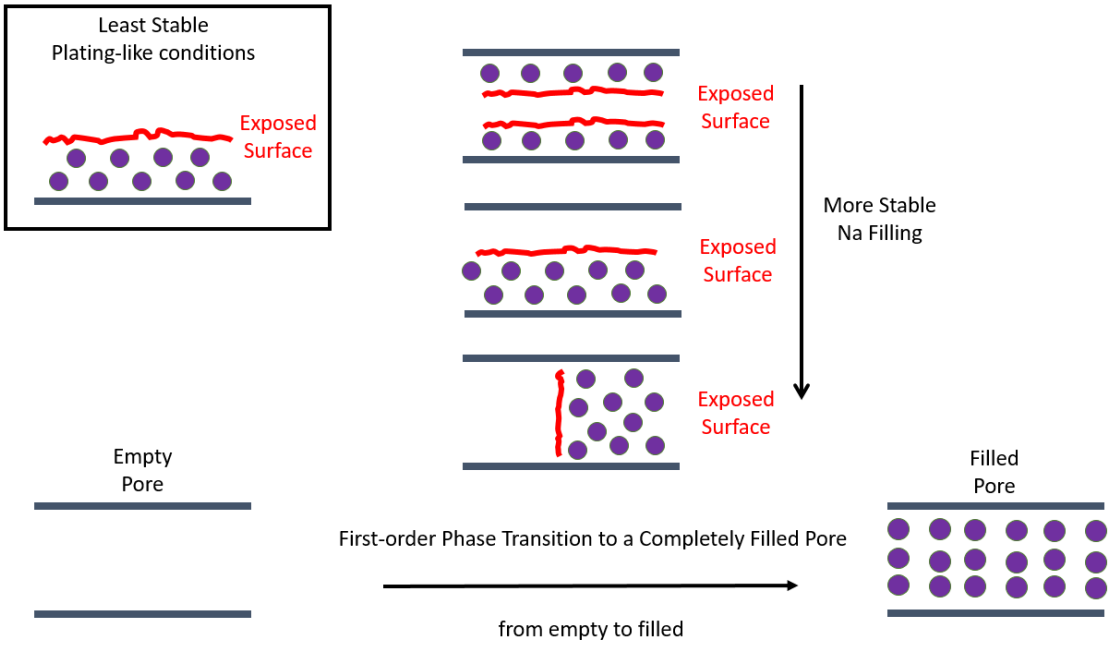

Supplementary Figure 33 | Schematic of the relative stabilities of various Na-pore phases. The first-order phase transition produces the flat voltage profile, matching the experimentally presented flat voltage.

Li and Na are constantly added as atoms throughout our investigation. Part of their valence electron density is donated to the carbon lattice during the DFT relaxation. The Li/Na atoms form clusters (non-metallic but quasi-metallic) as lithiation/sodiating progresses. Studying the calculated convex hull, we obtain the stability order during lithiation/sodiation presented in this Figure. We observe that Li/Na lowers its energy (more stable pore filling) by (a) clustering close to other Li/Na and (b) wetting (creating contacts) its exposed surfaces with the carbon walls. Thus, pore filling is a competition between nucleating Li/Na clusters and minimizing the energy penalty from exposed surfaces. Pores of the right size (0.7 to 1.4 nm) avoid significant Li/Na clustering that drops the potential below zero and eventually leads to plating.

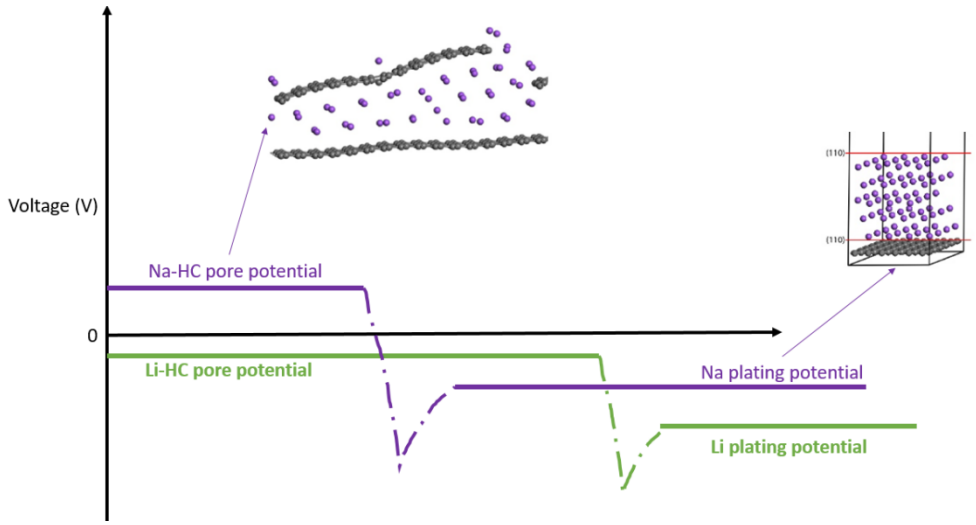

Supplementary Figure 34 | Comparison between pore filling and plating for Na and Li in HC with DFT. Please be aware that the plateau refers only to the pore-filling and not the edge surface adsorption.

Comparing the calculated plating potentials (Li/Na layering on top of graphene, supplementary Figure 32) and the potential in the sodiated pore (Figure 3 in Main text), we form this Figure to provide a more clear explanation. The above figure hints toward an optimal pore size for the electrochemical process. If the closed pores are too large, the graphene sheets of the wedge-pore are too far apart, and the exposed quasi-metallic Li/Na surface will likely drop the voltage below the 0 V cutoff before the pore filling manages to wet the whole surface, limiting the offered capacity. For large pores, Na will practically feel the environment shown in the right subfigure of supplementary Figure 33, where plating occurs. On the other hand, for optimum pore sizes described in the manuscript, wetting of Na with the carbon phases will form the configuration shown in the left subfigure above, for which the calculated potential is higher than the plating potential. These results are consistent both for Li and Na and match experimental voltage curves that show the plating potential occurring after the plateau stage in both cases once the nucleation potential ("V" shape) is encountered. This is also supported by experiments showing a maximum capacity with increasing pore size[29] and other DFT calculations[30] that show positive potentials for 2-5 layers and negative potentials for larger layering in the pore.

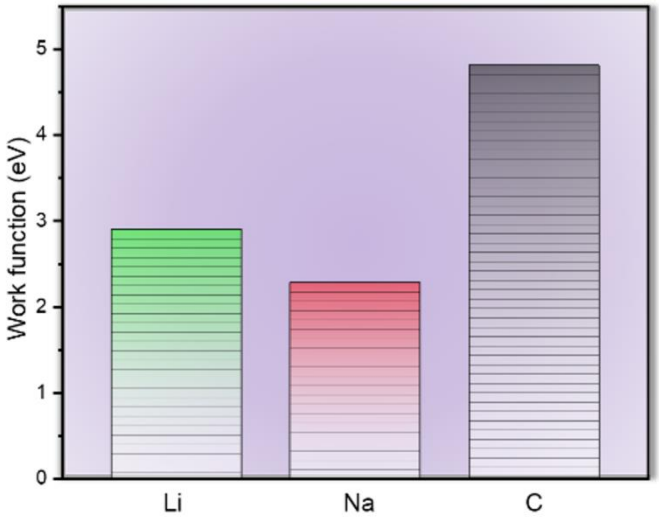

Supplementary Figure 35 | Work function values of lithium, sodium, and carbon.

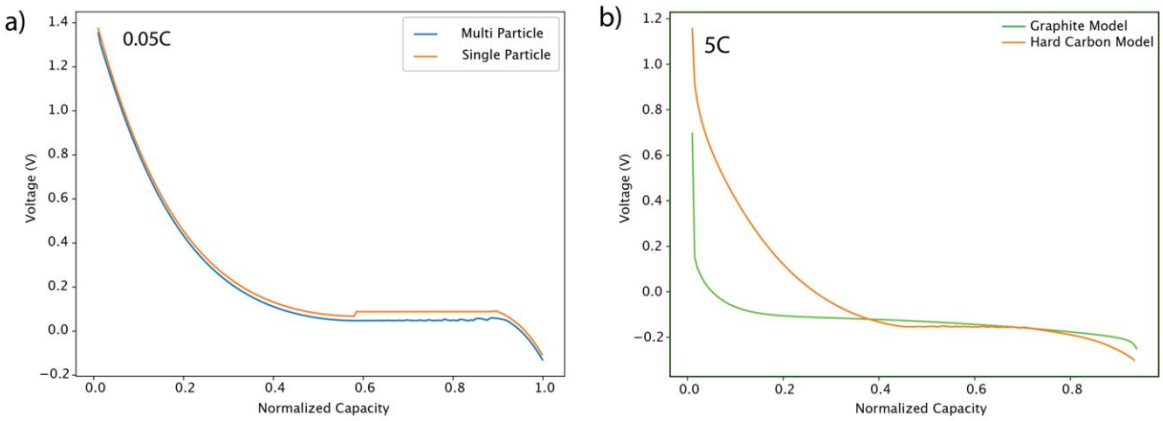

Supplementary Figure 36 | a, sodium insertion of hard carbon at 0.05C, comparison between multi-particle simulation and single particle. b, 5C sodium insertion (orange line) of hard carbon and 5C lithium insertion in graphite (green line), keeping the same morphological features.

The low-rate sodium insertion was simulated both considering a single particle and an ensemble of 30 particles. The results in Supplementary Figure 36 are in agreement with

the experiments, also showing how the collective system does not show the typical voltage drop of phase-separating materials due to the inter-particle interactions.

A comparison between a half-cell sodium insertion of the hard carbon and a half-cell lithiation of graphite was made at 5C. From Supplementary Figure 36b it is clear how the graphite voltage will stay below 0 for the entire lithiation while only at ~40% of the SOC the hard carbon will break the 0V line.

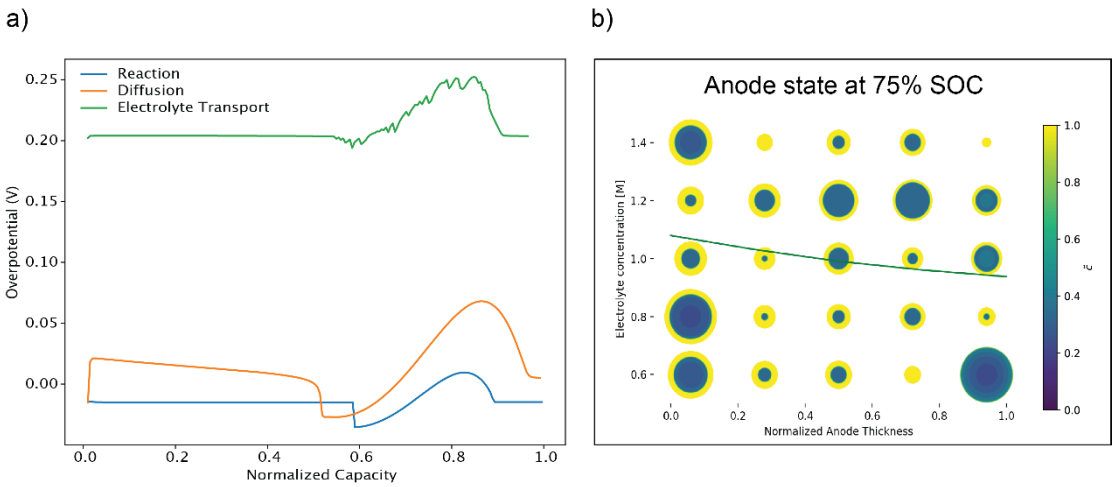

Supplementary Figure 37 | a, Deconvolution of the various sources of overpotentials at 5C. To break down the overpotential contributions, we followed the same method as in reference 1. b, Anode cross section showing the ability of the model to capture the correct physics of the material. Solid solution slope and phase separation plateau regions. The $\tilde{c}$ refers to the ratio between Na concentration and the maximum concentration used in our experiment, which does not coincide with the fully saturated Na density.

Finally, thanks to the simulations, it is possible to deconvolute the various sources of overpotential. Supplementary Figure 37a shows how the main reason why the overpotential drops below 0 for the case of hard carbon is the ionic transport overpotentials in the electrolyte. In particular, the reaction overpotential (blue line) is lower than the estimated nucleation barrier for the Na plating (as shown in Figure 2 of the main text).

Looking at the latest studies of Li metal plating[31], it is underlined how the main driving force for plating is not to be found in the overall voltage dropping below 0, but in the diffusion limitations which bring the concentration at the surface of the particle close to the maximum filling fraction and in the reaction overpotential, we can conclude that the model also shows how the material, thanks to its high diffusivity and its low insertion energy barrier, avoids Na plating even at high insertion rates such as 5C. Moreover, the limited amount of time the anode potential drops below 0 further prevents the kinetically limited plating from forming. If a different morphology were to be utilized, the diffusion overpotentials, already significant in the phase-separation zone, would drive the sodium concentration at the interface close to the maximum packing, promoting Na plating. Moreover, in different, less optimized morphologies, the reaction overpotentials arising from the particles' lower specific surface area would exceed the nucleation barrier for Na plating, inducing faster plating kinetics.

The model thus shows how the specific morphology obtained in this work improves the cycle life at a high rate of the presented battery. More specific studies dedicated to mesoscale modeling of amorphous hard-carbon systems are advised to provide more accurate quantitative results.

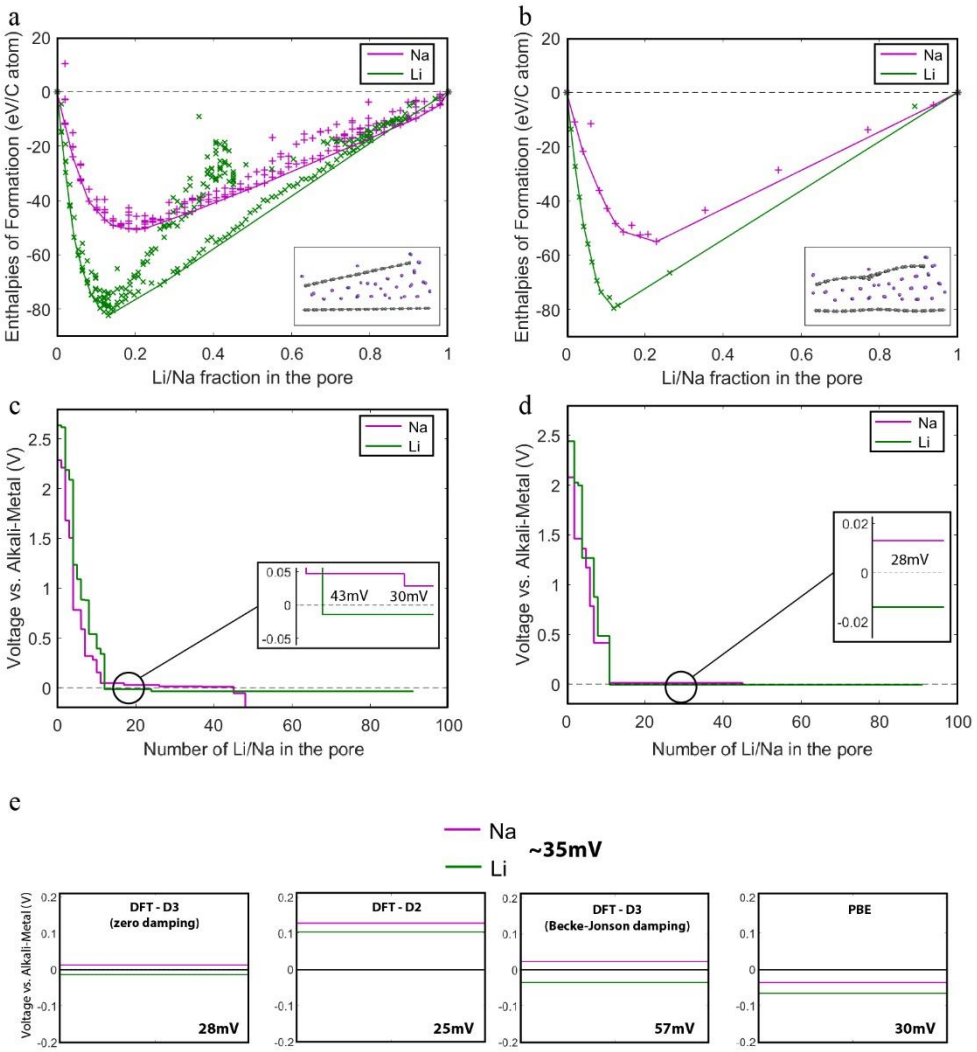

Supplementary Figure 38 | Relaxation and Energy of the Wedge Pore. a, Convex hull of the first relaxation step where only Na is allowed to relax, keeping the carbon matrix frozen. b, From the most stable points (convex line) of the first step, we construct the convex hull (second optimization step) where both carbon matrix and Na can relax. c, d. The Li/Na voltage profiles from the first and second optimization steps, respectively. e, Evaluation of the accuracy of DFT calculations. The plateau region of the second optimization step was calculated with four different DFT methods. Even though the absolute values of the plateaus marginally change, the relative difference between Li and Na remains consistent (Na plateau is higher than Li, ~35 mV).

Supplementary details of simulations:

The structural complexity of hard carbon presents a challenge in our study. Therefore, we initially aim to simplify it by breaking down the system into configurations suitable for DFT simulations, leading to the wedge-pore configurational system that includes several environments encountered in hard carbon in the same structure (vacancy, edge, and pore with semi-parallel sheets).

(1) Graphene edge calculations

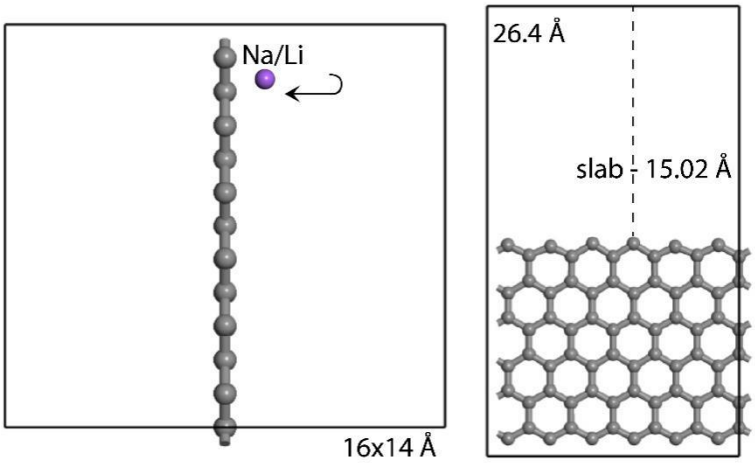

Supplementary Figure 39 | Graphene edge configurational environment.

In Supplementary Figure 39, we employ a slab configuration in which the graphene sheet (72 carbon atom supercell) is parallel to the vacuum, exposing two edges as per periodic boundary conditions. The slab introduces a vacuum of more than 15 Å to avoid self-interactions. Stepwise, we introduce Na/Li atoms in inequivalent and energy-competing configurations for geometry and energy optimization, employing the computational parameters indicated in the methods section of the main manuscript. We cover all the sodiation/lithiation range until the edge is completely packed with Na/Li. Following the formulation presented in the Methods, we construct voltage profiles following the lowest enthalpy path.

(2) Interface effects and encapsulated configurations

Next, to investigate the Na/Li surface and interface effect in a pore environment, we sodiated/lithiated a pristine graphene sheet perpendicular to the slab, as depicted in Supplementary Figure 40.

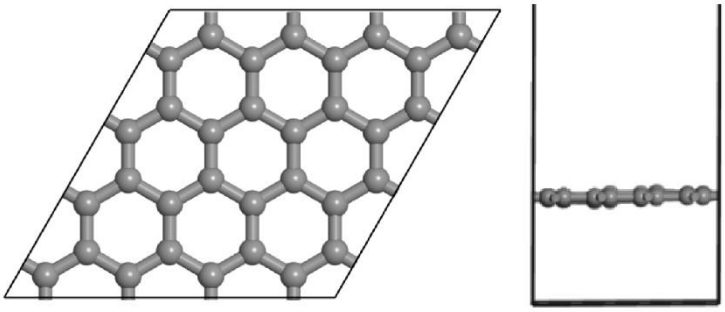

Supplementary Figure 40 | Pristine graphene sheet perpendicular to the slab.

We introduced stepwise Na/Li atoms on the pristine surface in inequivalent and energy-competing configurations for geometry and energy optimization. In Supplementary Figure 41, our results indicate that Na/Li cluster together, forming a (110) monolayer at negative formation voltages. We subsequently introduced more (110) layers (up to five) to examine the evolution of the voltage upon a process that resembles plating (Supplementary Figure 41). We observe that more layers stabilize the structure, raising the voltage approaching 0 V vs. Na metal (-0.05 V).

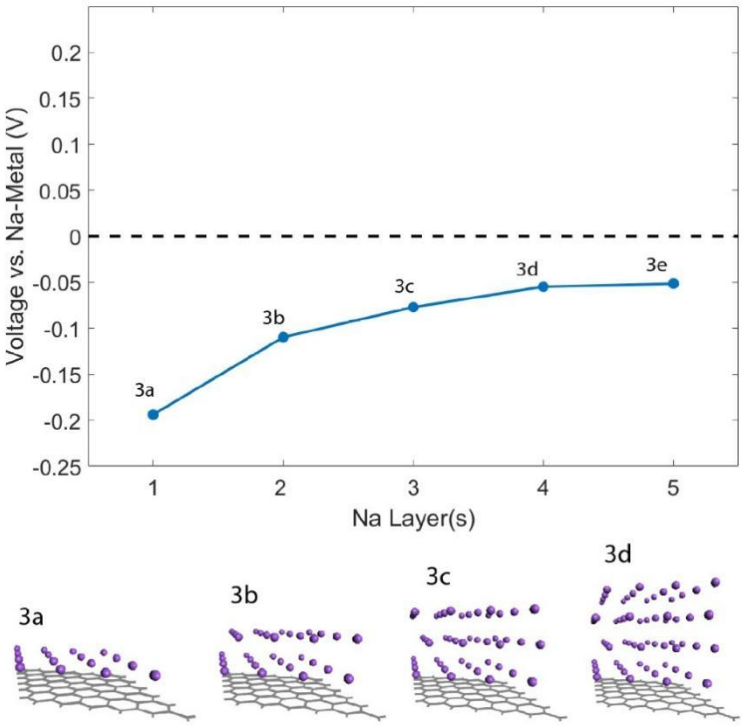

Supplementary Figure 41 | Voltage vs. Na-metal of multilayer Na layer deposition (plating on graphene) and the respective configurations

To compare the energetics and formation voltages of the plated (layers on graphene) configurations shown above with (1) isolated clusters of Na/Li layers and (2) Na/Li layers "sandwiched" by graphene (layers in the pore), we (1) deleted the graphene layer and (2) introduced a second graphene layer "sandwiching" the structure, respectively. We then repeated the geometry and energy optimization for the one to five Na/Li layers, where the results are presented in Supplementary Figure 32.

(3) Wedge Pore calculations

Finally, we construct a more realistic hard carbon configuration (wedge pore), depicted in Supplementary Figure 26, that includes vacancy, edges, and pore environments to demonstrate the full sodiation/lithiation process. The periodic boundary conditions are indicated by the lines indicating the simulated cell. Hard carbon is known for its intricate blend of curved graphene and fullerene-like structures. This network creates nanopores of varying sizes and distributions and we employ curved and misaligned nanopore configurations with exposed edges and defects, reflecting realistic nanopore

sizes. These configurations effectively capture the interaction environment within the pore and enable the study of slope-to-plateau transitional behavior. The sodiation/lithiation process was again simulated by inserting Na/Li in inequivalent and energy-competing configurations until the vacancy, edge, and pore environments were completely full.

Modelling the pore environment presents computational challenges because of its size. To address this, in the first optimization step, we freeze the carbon atoms and let Na/Li atoms relax. Subsequently, we relax the most stable configurations of the "frozen" convex hull to let all atoms relax toward the lowest energy position. We present results for both the frozen carbon matrix and fully relaxed configurations, providing insights into nonplastic (buried nanopore) and flexible plastic ones.

The calculation scheme is presented in Supplementary Figure 42.

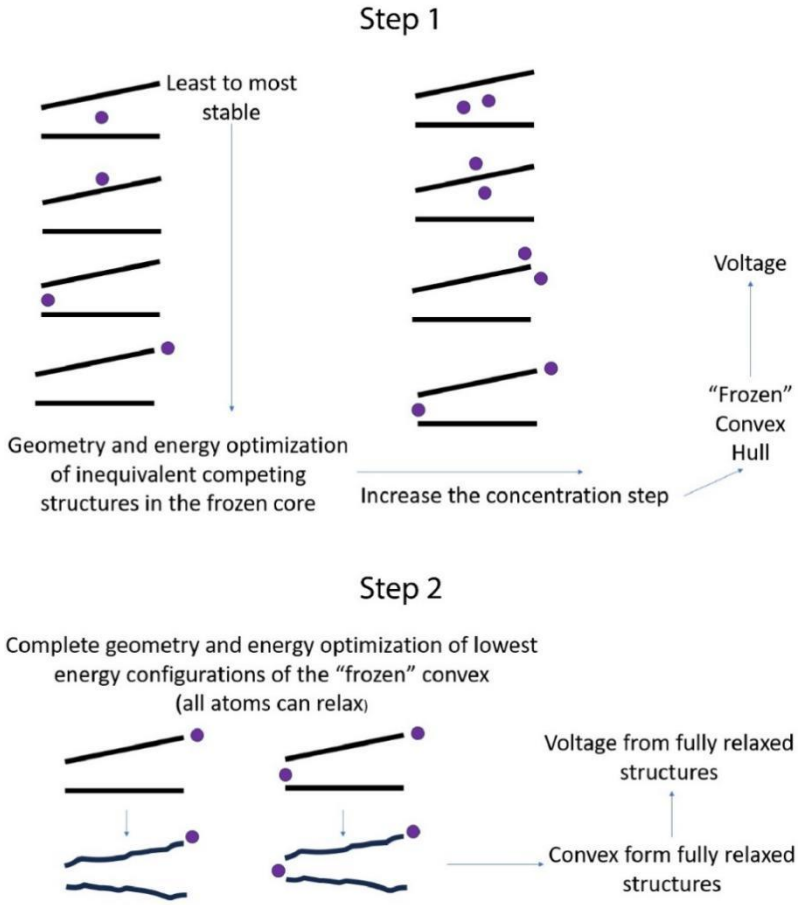

Supplementary Figure 42 | Scheme of our DFT calculations.

(4) Molecular Dynamics Calculations

A 1 x 2 x 1 supercell configuration of the structure presented in Supplementary Fig. 26 with dimensions 37 x 14.8 x 30 Å with a total of 334 C and 52 Na diffusing atoms was tested with MD simulations. (AIMD) calculations were performed using 400 eV and 1 x 1 x 1 cutoff energy and k-point mesh, respectively. All simulations were performed within the NVT computational ensemble and utilized a 2 fs time step and a 2.5 ps equilibration time. We selected to study the pore at 50% capacity for this calculation. In this way, we can determine whether Na atoms can move sufficiently fast in the nanopore environment within the timeframe of the ultra-high currents measured herein experimentally. Due to the large size of the realistic investigated pore, a quantitative analysis was not feasible, obtaining a simulation time of 18 ps at 600 K.

(5) Bader Charge

For the purposes of Bader charge determination, we performed accurate subsequent self-consistent energy calculations to the relaxed configurations of interest.

(6) Mesoscale Phase Field Modelling

In this final step, we move away from nanoscale ab intio simulations and construct a mesoscale phase-field model incorporating experimental and computed characteristics of our electrochemical system into an advanced python-based simulation package capable of capturing both kinetics and thermodynamics of active materials[32]. The modifications, process and key equations utilised are mentioned in the methods section of the main text.

Supplementary Table 1 | Surface energy of Li/Na/K.

Metal	Surface Energy of the (110) surface (j/m^2)	Experimental (j/m^2)	Other Theoretical Results (j/m^2)
Li	0.571	0.522[33]	0.585[34] 0.556[35]
Na	0.320	0.261[33]	0.247[34] 0.253[35]
K	0.152	0.145[33]	0.137[34] 0.135[35]

Supplementary Table 2 | The parameter comparison between our NIBs based on HCS-1200 and other NIB electrochemical technologies for grid energy storage.

Anode & cathode materials	Mass loading of anode (mg/cm^2) @ electrode thickness (mm)	Energy density (Wh/kg)	Cell type & Capacity of full cell (Ah)	Charging protocol@ voltage window	Charging time of full cells (min) @ Capacity retention	Cycling lifetime of full cell at fast charging (rate@ times@ capacity retention)	Ref.
HCS-1200 + Layered oxide (IOP)	7-8 @ ~170 (double sided coating)	~110	Cylindrical cell ~3	CC @ 1.5-4 V	~9 @80%	+6.5C; −6.5C @3000 @83%	This work
Hard carbon + Layered oxide (Faradion)	5.29 @ 64 (single sided coating)	-	Pouch cell 0.006-0.01	CCCV @ -	~13+5 (CV) @68%	+4.54C; −1C @ 100 @-	36

Hard carbon + Layered oxide (Faradion)	-	~140	Pouch cell 12	CCCV @ 1-4 V	60 @~75%	+1C; −C/3 @600 @-	37
Hard carbon + Layered oxide (Natrium)	-	~95	Pouch cell 0.88	CC @ 1.5-3.8 V	60 @85%	+1C; −1C @2500 @80%	38
Hard carbon + Layered oxide (UOJ)	1.2-1.5 @ -	-	Pouch cell -	CC @ 1.8-3.4 V	60 @~92.6%	+1C; −2C @300 @~92.7%	39
Hard carbon + Polyanion -type (CNRS)	3-6 @ -	75	Cylindrical cell ~0.4	CC @ 2-4.25 V	60 @-	+1C; −1C @3750 @80%	40
Hard carbon + Polyanion -type (Tiamet)	-	~122	Cylindrical cell -	-	60 @-	+1C; −1C @4000 @90%	41
Hard carbon + Polyanion -type (Tiamet)	-	-	Cylindrical cell ~0.7-0.75	CC @ 2-4.3 V	10-11 @84	+5C; −5C @5 @-	42

Hard carbon + Prussian blue (UOW)	-	-	Pouch cell 7	CC @ 1-3.2 V	60 @~71%	+1C; −1C @1000 @78%	43
Hard carbon + Prussian blue (Novasis)	-	100-130	Pouch cell 0.5-5	CC @ 1.5-3.5 V	60 @<95%	+1C; −1C @500 @98.6%	44
Hard carbon + Prussian white (CATL)	-	~160	Pouch cell -	-	15 @80%	-	49

Supplementary Table 3 Parameters used for the multiphase porous electrode theory simulations.

Hard-carbon parameters	
OCV (c)	$1.435 - 7.6991\,c + 16.4064\,c^2 - 13.120\,c^3 - 8.1404\,c^4 + 22.754\,c^5 - 11.7639\,c^6$
Gradient penalty (κ_{Mn})	$4 \cdot 10^{-7}$ J/m
Charge transfer coefficient (α)	0.5
k_0	$50\ A/m^2$
Diffusivity	$2.5 \cdot 10^{-15}\ m^2 s$
Morphology	
Thickness (L)	~80 μm
Porosity	~50 %
Active material volume	95 %

loading	
Bruggeman coefficient	0.4

Electrolyte	
Concentration	1 M
Model	dilute
D_+	$2 \cdot 10^{-10}\ m^2/s$
D_-	$3 \cdot 10^{-10}\ m^2/s$

Supplementary Video 1 | Depiction of correlated diffusion in the pore.
The video depicts a Na atom approaching another Na atom. For distances below 4 Å the Na atoms associate and the Na pair diffuses together for 0.4 ps.

Supplementary Note 1

As the specific rate limiting step of fast charging including the transport of sodium inside the electrodes, ion transport within the electrolyte phase in the porous electrodes, etc., it is still controversial according to many recent literature[45, 46, 47, 48]. In order to confirm the limiting factor of Na-ion fast charging, we produced a mesoscale phase-field model to explore the kinetic limitations and contributions to the overpotential of our electrochemical system in Supplementary Figures 36 and 37. The mesoscale calculations make it clear that the Na plating is avoided due to the faradaic Butler Volmer contribution and Na concentration. The calculations underline that Na^+ ion diffusion in electrolyte through the anode thickness is the limiting factor but also explain why focusing on the anode morphology is important to avoid Na plating. The geometry and morphology of the electrode (which is affected by the hard carbon we present) will affect the interconnectivity of the pores lowering the resistance for Na transport in the electrolyte pores on the anode side. In addition, the small size of pores and their quasi-metallic character allow fast diffusion within the pores of the nanostructured active material.

Supplementary References:

1. Saurel D, *et al.* A SAXS outlook on disordered carbonaceous materials for electrochemical energy storage. *Energy Storage Materials* **21**, 162-173 (2019).

2. Dou X, *et al.* Hard carbons for sodium-ion batteries: Structure, analysis, sustainability, and electrochemistry. *Materials Today* **23**, 87-104 (2019).

3. Sadezky A, Muckenhuber H, Grothe H, Niessner R, Pöschl U. Raman microspectroscopy of soot and related carbonaceous materials: Spectral analysis and structural information. *Carbon* **43**, 1731-1742 (2005).

4. Saeidi N, Parvini M. Accuracy of Dubinin-Astakhov and Dubinin-Radushkevich adsorption isotherm models in evaluating micropore volume of bentonite. *Periodica Polytechnica Chemical Engineering* **60**, 123-129 (2016).

5. Stevens D, Dahn J. An in situ small-angle X-ray scattering study of sodium insertion into a nanoporous carbon anode material within an operating electrochemical cell. *Journal of The Electrochemical Society* **147**, 4428 (2000).

6. Li Y, *et al.* Regulating Pore Structure of Hierarchical Porous Waste Cork-Derived Hard Carbon Anode for Enhanced Na Storage Performance. *Advanced Energy Materials* **9**, 1902852 (2019).

7. Cançado LG, *et al.* General equation for the determination of the crystallite size La of nanographite by Raman spectroscopy. *Applied Physics Letters* **88**, 163106 (2006).

8. Wang C-Y, *et al.* Fast charging of energy-dense lithium-ion batteries. *Nature*, (2022).

9. Huang J, *et al.* Operando decoding of chemical and thermal events in commercial Na(Li)-ion cells via optical sensors. *Nature Energy* **5**, 674-683 (2020).

10. Zheng Y, Wang Y, Lu Y, Hu Y-S, Li J. A high-performance sodium-ion battery enhanced by macadamia shell derived hard carbon anode. *Nano Energy* **39**, 489-498 (2017).

11. Zheng Y, *et al.* Superior electrochemical performance of sodium-ion full-cell using poplar wood derived hard carbon anode. *Energy Storage Materials* **18**, 269-279 (2019).

12. Zhang SS. The Puzzles in Fast Charging of Li-Ion Batteries. *Energy & Environmental Materials* **5**, 1005-1007 (2022).

13. Stevens DA, Dahn JR. The Mechanisms of Lithium and Sodium Insertion in Carbon Materials. *Journal of The Electrochemical Society* **148**, A803 (2001).

14. Li Y, *et al.* Amorphous monodispersed hard carbon micro-spherules derived from biomass as a

high performance negative electrode material for sodium-ion batteries. *Journal of Materials Chemistry A* **3**, 71-77 (2015).

15. Jayaraman S, *et al.* Li-ion vs. Na-ion capacitors: A performance evaluation with coconut shell derived mesoporous carbon and natural plant based hard carbon. *Chemical Engineering Journal* **316**, 506-513 (2017).

16. Xiang J, Lv W, Mu C, Zhao J, Wang B. Activated hard carbon from orange peel for lithium/sodium ion battery anode with long cycle life. *Journal of Alloys and Compounds* **701**, 870-874 (2017).

17. Komaba S, *et al.* Electrochemical Na Insertion and Solid Electrolyte Interphase for Hard-Carbon Electrodes and Application to Na-Ion Batteries. *Advanced Functional Materials* **21**, 3859-3867 (2011).

18. Soto FA, *et al.* Tuning the Solid Electrolyte Interphase for Selective Li- and Na-Ion Storage in Hard Carbon. *Advanced Materials* **29**, 1606860 (2017).

19. Yamamoto H, *et al.* Synthesizing higher-capacity hard-carbons from cellulose for Na- and K-ion batteries. *Journal of Materials Chemistry A* **6**, 16844-16848 (2018).

20. Kubota K, *et al.* Structural analysis of sucrose-derived hard carbon and correlation with the electrochemical properties for lithium, sodium, and potassium insertion. *Chemistry of Materials* **32**, 2961-2977 (2020).

21. Ajuria J, Redondo E, Arnaiz M, Mysyk R, Rojo T, Goikolea E. Lithium and sodium ion capacitors with high energy and power densities based on carbons from recycled olive pits. *Journal of Power Sources* **359**, 17-26 (2017).

22. Huang S, *et al.* N-Doping and Defective Nanographitic Domain Coupled Hard Carbon Nanoshells for High Performance Lithium/Sodium Storage. *Advanced Functional Materials* **28**, 1706294 (2018).

23. Au H, *et al.* A revised mechanistic model for sodium insertion in hard carbons. *Energy & Environmental Science* **13**, 3469-3479 (2020).

24. Li Q, *et al.* Sieving carbons promise practical anodes with extensible low-potential plateaus for sodium batteries. *National Science Review*, (2022).

25. Yu J, *et al.* A class of liquid anode for rechargeable batteries with ultralong cycle life. *Nature Communications* **8**, 14629 (2017).

26. Wang Z, *et al.* Probing the Energy Storage Mechanism of Quasi-Metallic Na in Hard Carbon for Sodium-Ion Batteries. *Advanced Energy Materials* **11**, 2003854 (2021).

27. Qiu S, *et al.* Manipulating Adsorption-Insertion Mechanisms in Nanostructured Carbon Materials for High-Efficiency Sodium Ion Storage. *Advanced Energy Materials* **7**, (2017).

28. Ozhabes Y, Gunceler D, Arias T. Stability and surface diffusion at lithium-electrolyte interphases with connections to dendrite suppression. *arXiv preprint arXiv:150405799*, (2015).

29. Kubota K, *et al.* Structural Analysis of Sucrose-Derived Hard Carbon and Correlation with the Electrochemical Properties for Lithium, Sodium, and Potassium Insertion. *Chemistry of Materials* **32**, 2961-2977 (2020).

30. Youn Y, Gao B, Kamiyama A, Kubota K, Komaba S, Tateyama Y. Nanometer-size Na cluster formation in micropore of hard carbon as origin of higher-capacity Na-ion battery. *npj Computational Materials* **7**, 48 (2021).

31. Gao T, *et al.* Interplay of lithium intercalation and plating on a single graphite particle. *Joule* **5**, 393-414 (2021).

32. Smith RB, Bazant MZ. Multiphase porous electrode theory. *Journal of The Electrochemical Society* **164**, E3291 (2017).

33. Tyson WR, Miller WA. Surface Free-Energies of Solid Metals - Estimation from Liquid Surface-Tension Measurements. *Surf Sci* **62**, 267-276 (1977).

34. Wang J, Wang SQ. Surface energy and work function of fcc and bcc crystals: Density functional study. *Surf Sci* **630**, 216-224 (2014).

35. Vitos L, Ruban AV, Skriver HL, Kollar J. The surface energy of metals. *Surf Sci* **411**, 186-202 (1998).

36. Rudola A, Wright CJ, Barker J. Communication—Surprisingly High Fast Charge Volumetric Capacities of Hard Carbon Electrodes in Sodium-Ion Batteries. *Journal of The Electrochemical Society* **168**, 110534 (2021).

37. Rudola A, *et al.* Commercialisation of high energy density sodium-ion batteries: Faradion's journey and outlook. *Journal of Materials Chemistry A* **9**, 8279-8302 (2021).

38. Che H, *et al.* Engineering optimization approach of nonaqueous electrolyte for sodium ion battery with long cycle life and safety. *Green Energy & Environment* **6**, 212-219 (2021).

39. Liang L, *et al.* Comparative investigations of high-rate NaCrO2 cathodes towards wide-temperature-tolerant pouch-type Na-ion batteries from −15 to 55 °C: nanowires vs. bulk. *Journal of Materials Chemistry A* **7**, 11915-11927 (2019).

40. Broux T, *et al.* High Rate Performance for Carbon-Coated Na3V2(PO4)2F3 in Na-Ion Batteries. *Small Methods* **3**, 1800215 (2019).

41. Tarascon J-M. Na-ion versus Li-ion Batteries: Complementarity Rather than Competitiveness. *Joule* **4**, 1616-1620 (2020).

42. Desai P, Abou-Rjeily J, Tarascon J-M, Mariyappan S. Practicality of methyl acetate as a co-solvent for fast charging Na-ion battery electrolytes. *Electrochimica Acta* **416**, 140217 (2022).

43. Wang W, *et al.* Reversible structural evolution of sodium-rich rhombohedral Prussian blue for sodium-ion batteries. *Nature Communications* **11**, 980 (2020).

44. Bauer A, Song J, Vail S, Pan W, Barker J, Lu Y. The Scale-up and Commercialization of Nonaqueous Na-Ion Battery Technologies. *Advanced Energy Materials* **8**, 1702869 (2018).

45. Liu Y, Zhu Y, Cui Y. Challenges and opportunities towards fast-charging battery materials. *Nature Energy* **4**, 540-550 (2019).

46. Cai W, *et al.* A review on energy chemistry of fast-charging anodes. *Chemical Society Reviews* **49**, 3806-3833 (2020).

47. Weiss M, *et al.* Fast Charging of Lithium-Ion Batteries: A Review of Materials Aspects. *Advanced Energy Materials* **11**, 2101126 (2021).

48. Yao Y-X, *et al.* Unlocking Charge Transfer Limitations for Extreme Fast Charging of Li-Ion Batteries. *Angewandte Chemie International Edition* **62**, e202214828 (2023).

49. Https://www.catl.com/en/news/665